Visible-Light Driven Heterojunction Photocatalysts for Water Splitting– A Critical Review

Savio J. A. Moniz,[1] Stephen A. Shevlin,[2] David James Martin,[1,2] Zheng-Xiao Guo[2] and Junwang Tang[1,*]

1. Department of Chemical Engineering, University College London, Torrington Place, London WC1E 7JE

2. Department of Chemistry, University College London, 20 Gordon Street, London WC1H 0AJ

*E-mail: Junwang.tang@ucl.ac.uk

Savio J. A. Moniz:

Dr Savio J. A. Moniz is a post-doctoral research associate working under the supervision of Junwang Tang in the Solar Energy Group in the Department of Chemical Engineering at UCL. Prior to this, he gained his PhD in Inorganic Chemistry at UCL Chemistry Department under Chris Blackman and Claire Carmalt working on MOCVD of multiferroic oxides for solar energy harvesting and computer memory storage. His current research focuses on the fabrication of thin film heterojunction photocatalysts for solar fuels synthesis and water purification.

Stephen A. Shevlin:

Dr Stephen Shevlin received an MSci from the University of Birmingham and a PhD from the Department of Physics at UCL under Andrew Fisher. He has worked extensively in the field of electronic structure calculations, working at IBM Zurich Switzerland, Oak Ridge National Laboratory, and Queen Mary, University of London. Currently he is working as a Senior Research Associate in the research group of Xiao Guo at the Department of Chemistry, UCL, and is focussing on the simulation of photocatalysts, clusters for green energy applications, and two-dimensional materials.

David James Martin

David James Martin studied Physics at the University of Liverpool (MPhys), and then completed a PhD in the Chemical Engineering Department at UCL under the supervision of Dr Junwang Tang. His thesis focussed on oxidation, reduction, and overall water splitting using visible light responsive photocatalysts. David is currently a UCL Chemistry research associate with Dr Andrew Beale. David's present work focuses on X-ray diffraction and scattering techniques for in-situ

characterisation of heterogeneous catalysts. His primary interests include photocatalysis for water splitting, heterogeneous catalysis, and in situ/operando methods for catalyst characterisation.

Zheng-Xiao Guo:

Xiao Guo is a Professor of Materials and Chemistry, leading a team of ~15 Postdocs and PhD students at UCL. Current research activities focus on the understanding and development of materials, nanostructures and processes to provide low-cost and efficient solutions for clean energy, particularly in energy harvesting, storage, CO_2 capture and biological fuel cells. He has contributed over 200 high-quality journal publications and over 30 conference papers/presentations in the field.

Junwang Tang:

Dr Junwang Tang is Reader in Energy at the Department of Chemical Engineering at UCL. He obtained his PhD in Physical Chemistry in 2001. After that, he was appointed as a JSPS fellow at NIMS, Japan, working on solar fuels synthesis and photocatalysis. He moved to the Department of Chemistry, Imperial College London as a senior Researcher in 2005 focusing on mechanistic studies of solar fuel synthesis by time-resolved spectroscopies and then joined UCL as a faculty staff member. His current research interests lie in solar fuel generation by artificial photosynthesis, mechanistic aspects of solar energy conversion, photocatalysis, biomaterials synthesis and microwave-assisted flow chemistry, resulting in nearly 100 publications and several international and domestic patents. He also sits on the editorial board of many journals and is a Fellow of the RSC.

TOC Image:

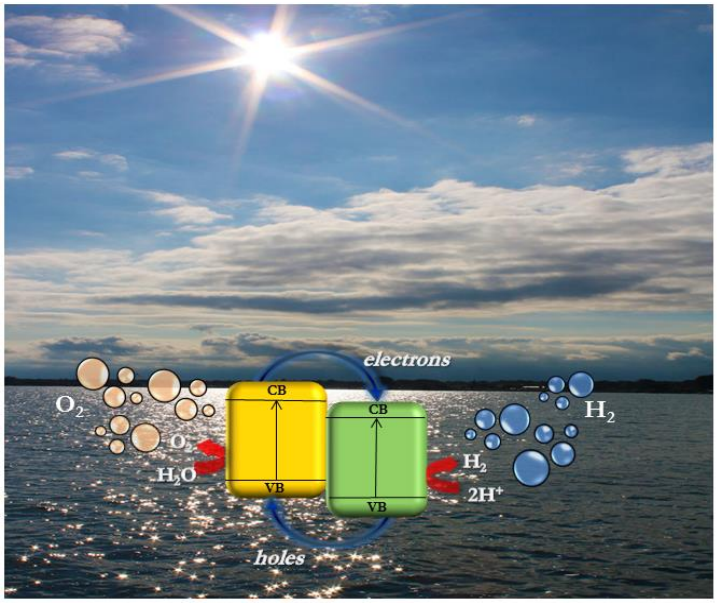

TOC Text: We summarise current state-of-the-art efficient visible-light driven heterojunction water splitting photo(electro)catalysts and describe how theoretical modelling of electronic structures at interfaces can explain their functionality.

Abstract

Solar driven catalysis on semiconductors to produce clean chemical fuels, such as hydrogen, is widely considered as a promising route to mitigate environmental issues caused by the combustion of fossil fuels and to meet increasing worldwide demands for energy. The major limiting factors affecting the efficiency of solar fuel synthesis include; i) light absorption, ii) charge separation and transport and iii) surface chemical reaction; therefore substantial efforts have been put into solving these problems. In particular, the loading of co-catalysts or secondary semiconductors that can act as either electron or hole acceptors for improved charge separation is a promising strategy, leading to the adaptation of a junction architecture. Research related to semiconductor junction photocatalysts has developed very rapidly and there are a few comprehensive reviews in which the strategy is discussed.[1,2,3] This *critical* review seeks to give an overview of the concept of heterojunction construction and more importantly, the current state-of-the art for the efficient, visible-light driven junction water splitting photo(electro)catalysts reported over the past ten years. For water splitting, these include $BiVO_4$, Fe_2O_3, Cu_2O and C_3N_4, which have attracted increasing attention. Experimental observations of the proposed charge transfer mechanism across the semiconductor/semiconductor/metal junctions and the resultant activity enhancement are discussed. In parallel, recent successes in the theoretical modelling of semiconductor electronic structures at interfaces and how these explain the functionality of the junction structures is highlighted.

Broader context.

Developing clean, low-cost and renewable fuel sources is a key challenge facing mankind in order to meet the energy demands of a growing population and increased industrialisation. The use of hydrogen as a fuel either through direct combustion or in a fuel cell is one method of producing clean energy with minimal impact to our environment. Hydrogen fuel can be harnessed by steam reforming of natural gas, a fossil fuel. A greener method of hydrogen generation is to split water into its components, hydrogen and oxygen. Electrolysis of water is one of the methods to produce H_2, however it is an energy intensive process. As an alternative, water reduction to hydrogen can be achieved by means of a semiconductor when driven by abundant solar energy. One of the key limiting

factors in these semiconductor photocatalysts is fast charge carrier recombination, but by way of other photocatalysts (or co-catalysts; following the concept of the junction structure), recombination can be suppressed and surface reactions for oxygen and/or hydrogen production can be accelerated. These junctions allow for efficient separation of electrons from holes, mimicking the pathway in natural photosynthesis. This strategy provides opportunities for much improved solar energy harvesting (e.g. photovoltaic devices) and high solar-to-hydrogen conversion efficiency, and hence could serve as the basis for the large scale manufacture of solar driven clean fuels in a zero carbon system.

1. Introduction to water splitting

With the ever increasing global reliance on non-renewable, geopolitically sensitive sources of energy, such as natural gas and coal, coupled with highly volatile crude oil prices, there has never been such an urgency to secure alternative clean, renewable energy supplies. Global primary energy consumption in 2013 was *ca*.17 TW, and is predicted to at least double by 2050. Currently nearly 90% of the global energy supply is generated from carbon-based fuels, and efforts to develop viable routes to solar fuels are thus of critical importance, i.e. *via* a light-driven electrochemical process. In particular, further understanding of the fundamental mechanism and kinetics of the processes occurring during artificial photosynthesis is needed in order to improve practical efficiency. The first reported splitting of water under solar irradiation utilised n-type TiO_2 coupled with a Pt counter electrode,[4] however due to its wide band-gap of 3.2 eV, it can only be excited by ultra-violet (UV) irradiation which accounts for just 4% of the solar energy reaching the Earth.[5] Therefore to utilise efficiently the energy of the solar spectrum, new visible-light responsive photocatalysts are required and are thus the main class of materials discussed in this review.[6] The constraints of choosing suitable photocatalysts for this process are limited to materials that not only possess appropriate band-gap positions that straddle the redox potentials of water splitting with a conduction band more negative than 0 V (vs NHE (Normal Hydrogen Electrode) at pH 0) and the valence band more positive than 1.23 V, but also exhibit appropriate surface reaction kinetics and reasonable stability in

aqueous solution under prolonged irradiation.[7] Thermodynamically, the water splitting reaction is an uphill process, requiring a minimum energy of 1.23 eV because the Gibbs free energy change for the reaction is $\Delta G° = 237.2$ kJ/mol or 2.46 eV/molecule of H_2O, and therefore requires high overpotentials. Nature itself demonstrates an efficient strategy to utilise solar irradiation (near unity quantum yield) by spatially separating electrons and holes in wireless photosynthesis reactions. The process of water splitting can be envisaged as two half reactions: water oxidation, and secondly, proton reduction to hydrogen fuel. Figure 1 summarises the different steps and their typical kinetics in water splitting.[8] Water oxidation is much more challenging because one molecule of gaseous oxygen requires four holes, and occurs on a timescale approximately five orders of magnitude slower than H_2 evolution, proven in both natural and artificial photosynthesis.[4] By means of spectroscopic techniques, the four hole water oxidation process has been shown to be the rate determining step during water cleavage (timescale of seconds) and competes with recombination, which takes place on the order of microseconds.

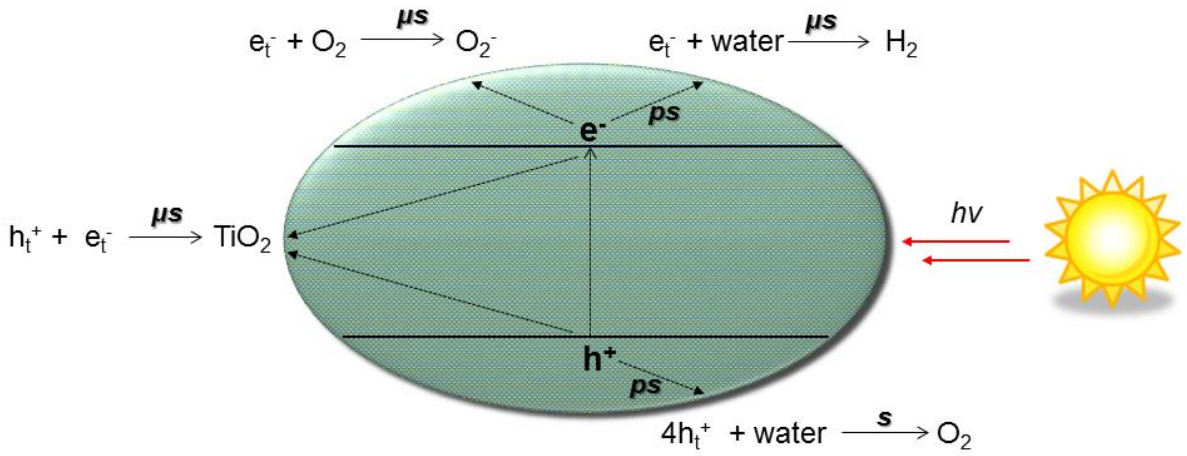

Figure 1: Mechanism of solar water splitting on TiO_2 measured by transient absorption spectroscopy.[8]

Numerous candidate materials have been reported but only for the half reactions (either water reduction or oxidation, e.g. Fe_2O_3,[9] WO_3[10,11] and $BiVO_4$)[12,13] with even fewer materials able to split water under visible irradiation; the fundamental steps of water splitting have been summarised in previous reviews,[1] and what is clear is that the efficiencies of suspension-based systems are too low at

present to develop commercially. One viable option is the development of photoelectrochemical cells to reduce water to H_2, where the anodic reaction will involve oxidation of water and therefore when coupled with the appropriate cathode/counter electrode (e.g. Pt), can drive proton reduction to H_2 under minimal applied bias.[6] The function of the electrical bias is to drive electrons from photocatalyst to counter electrode and therefore, to a certain extent, alleviate recombination effects and/or photocorrosion. Nevertheless, the current solar-to-hydrogen conversion efficiency (STH) is still too low to develop a commercial device for large-scale water splitting. A new materials strategy therefore is required to enhance the energy conversion efficiency. One of the key limiting factors affecting efficiency in artificial photosynthesis is recombination of charge carriers. After excitation from an incoming photon of suitably high energy, electron-hole pairs (excitons) are formed in the semiconductor; the electron is promoted from the valence band (VB) to the conduction band (CB), leaving behind a hole in the valence band. The hole and electron may migrate to the surface on the picosecond timescale and then take part in the appropriate oxidation/reduction reactions. It is this pathway and lifetime of the charge carriers which is critically important; if the carriers recombine faster than the expected reactions (which is the case for water splitting), the energy conversion efficiency is quite moderate. Thus for optimal efficiency the carriers should be separated as far as possible, or as long as possible, on the surface of a photocatalyst.

Suppression of charge recombination can be attempted in a number of ways: i) the use of scavengers (sacrificial solutions), which can remove either holes or electrons in the system so that only one half of the water splitting reaction can be studied in isolation (either reduction or oxidation);[14] ii) variation of the morphology of the photocatalyst, which has been shown to improve photocatalytic activity due to the increase in surface area and the shortening of charge carrier diffusion pathways to the surface;[15,16] and iii) the creation of a heterojunction, whereby charge-carriers are generated in one photocatalyst and subsequently vectorially transferred to the other material, allowing for long-lived electron-hole pairs, mimicking the mechanism exhibited in Photosystem II during artificial photosynthesis.[17,18] In theory, redox-level heterojunctions which employ an offset in the energies of the conduction and/or valance band edges allow for interfacial charge transfer from one

semiconductor to another. Indeed, two typical examples involving visible light-driven junctions for overall water splitting: $(Ga_{1-x}Zn_x)(N_{1-x}O_x)$ with RuO_x co-catalyst (suspension)[19] and GaAs/ GaInP architecture[20] (electrode) have successfully applied this principle.

2. Junction architectures

As stated earlier, for photoanode materials to partake in oxidation reactions, the top of the valence band must be more positive than the oxygen evolution potential whilst a p-type semiconductor (photocathode) requires a conduction band position more negative than the hydrogen evolution potential. A small external bias (electrical energy) can then be used to drive electrons to the counter electrode to improve charge separation.

To describe the various band alignments commonly found in junctions and junction composites, one must first introduce the three main types of heterojunction architectures (Figure 2), where A corresponds to semiconductor/component A, and B corresponds to semiconductor/component B (one should note that if they are semiconductors, they can be either n-type or p-type). A Type I heterojunction consists of (two) semiconductors whereby the the CB of component B is higher than that of A. The VB of B is lower than that of A, therefore holes and electrons will transfer and accumulate on component A.

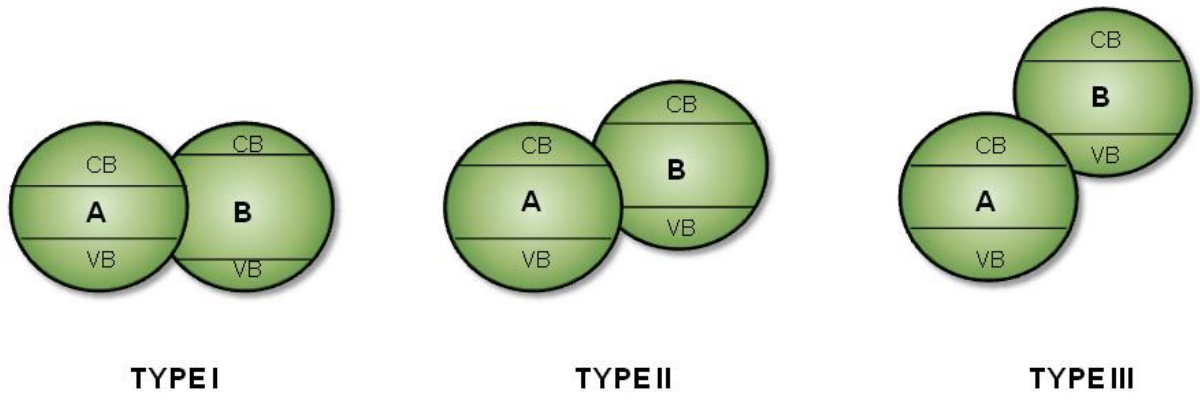

Figure 2: Band alignment in Type I, II, and III heterojunctions.

A type II junction relies on the transfer of photoexcited electrons from B to A due to the more negative CB position of B. Holes can travel in the opposite direction from the more positive VB of A

to B, leading to all-round efficient charge spearation and enhanced photocatalytic activity. The third type, Type III, is identical to Type II except for the much more pronounced difference in VB and CB positions which gives a higher driving force for charge transfer.[3]

To date, charge separation strategies have primarily centred on the use of semiconductor/electrolyte interfaces under the application of electrical bias. When a semiconductor electrode is immersed in an electrolyte solution, electron transfer takes place between the semiconductor and the electrolyte solution which results in equilibration of the Fermi level (E_f) to that of the redox potential of the electrolyte and thus is the basis of the semiconductor liquid junction (SCLJ).[21] Electron transfer processes at the interface of the semiconductor/electrolyte causes band-bending because electron density is absolute deep within a semiconductor and the band positions are pinned. This band bending is more pronounced for interfaces in close, intimate contact but less so when the space charge layer width is greater than the particle size, in the case of nanoparticles. Semiconductor–liquid interfaces are the most commonly employed type of junction for charge separation in water splitting and nanostructuring of the SCLJ has proven to be an effective approach to shorten the diffusion length of charge carriers.[22] Electron transfer can occur between the semiconductor and electrolyte when the Fermi level of the semiconductor is in the appropriate position (more positive/negative) than the potential of the electrolyte to then either accept/ donate electrons. The space-charge layer contributes to the formation of an electric field; in n-type materials (photoanodes), photoexcited holes accumulate on the surface of the semiconductor and are consumed in oxidation reactions, whilst electrons are transferred to a counter electrode *via* the back contact and an external circuit, and used in reduction reactions, such as proton reduction to H_2. Further information on band bending in semiconductors may be found in the recent review by Zhang and Yates.[23]

Recently heterojunctions formed between two solid materials have attracted more attention, including semiconductor-semiconductor S-S, semiconductor-metal S-M, and semiconductor-carbon S-C (carbon nanotubes, graphene, etc) heterojunctions.[24] By far the most commonly employed heterojunction is based on a S-S architecture, usually between a p-type and n-type semiconductor in close contact. A schematic representation of this junction is highlighted in Figure 3a. The result is a space-charge

region at the interface and an electric field induced as a result of diffusion of charge carriers. This can direct the flow of electrons to the CB of the n-type material and the holes can move to the VB of the p-type material, resulting in more efficient separation, longer charge carrier lifetimes and higher reaction rates. For S-M junctions (Figure 3b), a Schottky barrier is formed when a semiconductor is in close contact with a metal and the result is Fermi level alignment induced by electron flow from the material with the higher Fermi level to the lower level (e.g Pt/TiO_2). The metal effectively acts as an electron trap to receive photoelectrons from the semiconductor after excitation, improving charge carrier separation and reducing recombination, as charge cannot flow in the opposite direction (unlike in an ohmic contact). For S-C junctions, several types of carbon species have been utilised; carbon nanotubes (CNTs) and graphene are the most comonly used due to their metallic-like conductivity, high electron mobility and high surface area, allowing for facile electron injection from the light absorbing semiconductor; a similar analogy to the S-M junction is obtained. The use of graphene-based junctions are reported in several recent reviews and will therefore not be discussed in detail here in this introduction.[25,26] Furthermore, multicomponent, "sandwich" junctions (e.g. CdS-Au-TiO_2)[27] have been employed to further effect charge separation and showed better photocatalytic activity compared to the bi-junctions CdS/TiO_2 and Au/TiO_2. These may have unusual charge transfer mechanisms. Many of the individual materials used for water splitting (oxidation/reduction) in both suspension and electrode systems have been covered in some detail in a number of recent review papers.[1,3,28]

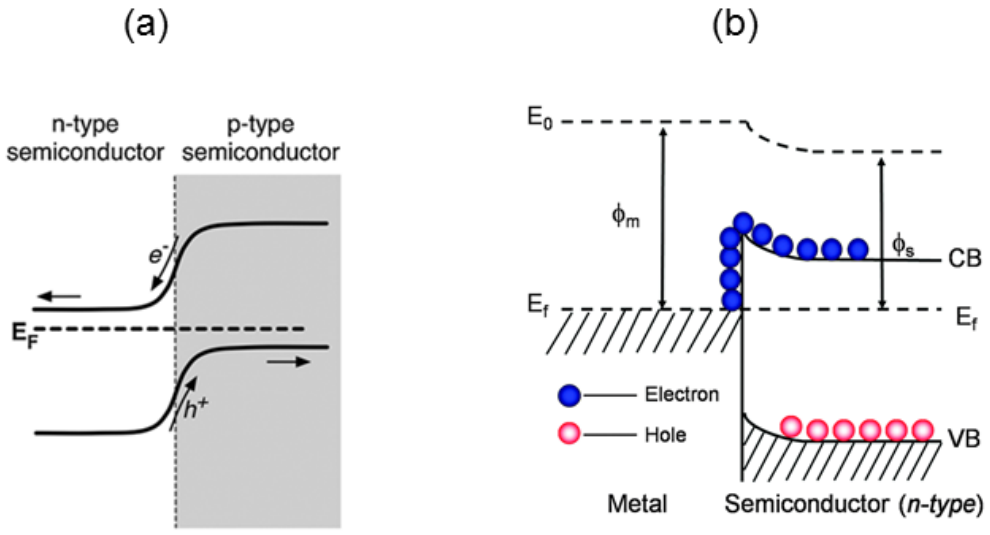

Figure 3: Band-bending and alignment in (a) S-S, and (b) S-M (S-C) junctions. In both cases photo-generated charges are driven in opposite directions due to favourable differences in band energies and the formation of an electric field. Reproduced from Refs. [29] **and** [30] **with permission from The Royal Society of Chemistry.**

Hence we are keen to address this concept of a heterojunction strategy to improve the efficiency of photocatalytic water splitting by combining two or more simple materials that already possess appreciable visible light absorption, high efficiency and reasonable stability - oxides, nitrides, sulphides and phosphates in both PEC and suspension systems. Indeed there has been some progress in the use of complex oxides (Rh-$SrTiO_3$,[31] $PbBi_2Nb_2O_9$,[32] $Sr_{1-x}NbO_3$[33] and oxynitrides ($SrNbO_2N$,[34] $LaTiO_2N$,[35] and TiON[36]) for overall water splitting under visible light but these materials are either difficult to synthesise in pure form, or the efficiencies reported are comparatively moderate. However one of the most promising, but lesser studied oxynitrides for overall water splitting under visible light is TaON (CBE at -0.3 V *vs* NHE, pH 0), which has recently received much attention through its incorporation into a heterojunction, for example with $CaFe_2O_4$,[37] N-doped TiO_2[38] and Cu_2O.[39] It is clear that transition metal oxynitrides have great potential in the future for utilization in water splitting systems, however more research into this emerging family of photocatalyst materials is required, particularly their incorporation into junction architectures, before we can truly assess their impact in this field.

We have thus summarised the main visible light driven heterojunction photocatalysts reported very recently that have the greatest potential to be used for large-scale water splitting. We also summarise the main experimental techniques used to measure important kinetic parameters such as charge separation efficiency and carrier lifetimes in these candidate materials. In addition, we review the current progress in the emerging field of computational prediction of semiconductor band alignment in order to predict and explain junction functionality and surface reactivity. Therefore the current review will complement the previous reviews which either summarise results[2,40] or focus on only single visible driven photocatalyst development.[41] The next section will primarily talk about oxygen evolution photocatalyst-based junctions and then go on to discuss hydrogen evolution photocatalyst-based junctions.

3. Visible-light responsive junctions

3.1 $BiVO_4$- based junctions

$BiVO_4$ has attracted widespread attention as a highly responsive visible-light driven photocatalyst for water oxidation in both suspension and PEC systems;[14] it possesses a band-gap of 2.4 eV with the VB edge (VBE) located at *ca.* 2.4 V *vs.* RHE (Reference Hydrogen Electrode), which provides sufficient overpotential for photoholes to oxidize water. However the CB edge (CBE) is located just under the thermodynamic level for proton reduction to H_2.[42] Recently a 4.9% solar-to hydrogen (STH) efficiency was reported for a gradient doped W:$BiVO_4$ photoanode connected to a Si solar cell in tandem configuration for water splitting.[43] Nevertheless, numerous groups have attempted to improve the STH conversion efficiency of $BiVO_4$, most notably through coupling with other semiconductors in an S-S junction. Progress in developing $BiVO_4$ photoanodes for water splitting has recently been covered in a comprehensive review.[44] Nevertheless, we have attempted to summarise the recent key results in junctions containing $BiVO_4$ (Table 1).

Table 1: Summary of recent key advances in $BiVO_4$ based heterojunction photocatalysts for PEC water splitting.

Junction	Synthetic method	Maximum	IPCE	STH values	Ref.

		photocurrent	value at 400 nm		
$BiVO_4/WO_3$	Spin-coating/solvothermal	~1.6 mA/cm^2 (1 V *vs* Pt CE)	31%	-	[45]
$BiVO_4/WO_3$	Polymer-assisted deposition	1.74 mA/cm^2 (0.7 V *vs* Ag/AgCl)	37%	-	[46]
$BiVO_4/SnO_2/WO_3$	Spin-coating	2.5 mA/cm^2 (1.23 V *vs* RHE)	~40%	1.35%	[47]
Co-Pi/$BiVO_4/WO_3$	Glancing-angle deposition	~3 mA/cm^2 (1.23 V *vs* RHE)	60%	-	[48]
Co-Pi/W:$BiVO_4$	Spray pyrolysis	~3.6 mA/cm^2 (1.23 V *vs* RHE)	-	4.9% (with Si solar cell)	[43]
FeOOH-NiOOH/(W,Mo)-$BiVO_4/WO_3$	Oblique angle deposition/drop-casting	5.35 mA/cm^2 (1.23 V *vs* RHE)	>90%	-	[49]
Co-Pi/$BiVO_4$/ZnO	Hydrothermal/spray pyrolysis	~3 mA/cm^2 (1.23 V *vs* RHE)	~47%	0.88%	[50]
$BiVO_4$/Al-ZnO	Polymer templating/dip-coating	1.5 mA/cm^2 (1.23 V *vs* RHE)	29%	-	[51]
Co-Pi/Mo-$BiVO_4$	Spin-coating	1.1 mA/cm^2 (1.1 V *vs* Ag/AgCl)	~65%	-	[52]
Co-Pi/Mo-$BiVO_4$	Spin-coating	~2.5 mA/cm^2 (1.23 V *vs* RHE)	-	-	[53]
Co-Pi/$BiVO_4$	Spray pyrolysis	~1.7 mA/cm^2 (1.23 V *vs* RHE)	-	2.1% (with solar cell)	[54]
FeOOH/$BiVO_4$	Electrodeposition	~2 mA/cm^2 (1.23 V *vs* RHE)	~45%	-	[55]
FeOOH-NiOOH/$BiVO_4$	Electrodeposition/drop-casting	~4 mA/cm^2 (1.23 V *vs* RHE)	60%	1.75% (ABPE)	[56]
Ni-B/$BiVO_4$	Spin-coating	~1.25 mA/cm^2 (1.23 V *vs* RHE)	30%	-	[57]

a) $BiVO_4/WO_3$

There are several reports of $BiVO_4/WO_3$ junctions for water splitting because WO_3 is a reasonably stable n-type semiconductor and the position of its CB edge (+0.42 V *vs* RHE) allows for facile electron injection from the CB of $BiVO_4$.[53, 58] $BiVO_4/WO_3$ nanorod array electrodes were grown by

Grimes and co-workers[45] who demonstrated improved IPCE (Incident Photon to Current Efficiency) values at 420 nm, increasing from 9.3% to 31% compared to planar films as a result of facile electron transfer from $BiVO_4$ to WO_3. Lee *et al.*[46] have demonstrated that a composite electrode consisting of $BiVO_4$ coupled to four WO_3 layers exhibited a 74% increase in photocurrent relative to bare WO_3, and 730% relative to bare $BiVO_4$, with almost a four-fold increase in IPCE at 425 nm (to *ca.* 37%). This is due to electron transfer from $BiVO_4$ to WO_3 and this strategy overcomes the poor charge transport observed for $BiVO_4$. Similarly, Sayama *et al.*[47] observed that coupling $BiVO_4$ with WO_3 and inserting a SnO_2 layer in between resulted in enhanced photocurrent (*ca.* 2.5 mA/cm^2 at 1.23V *vs* RHE), significantly higher than their $BiVO_4/WO_3$ and the individual materials when tested in carbonate electrolyte. The Fermi level of SnO_2 is located between those of $BiVO_4$ and WO_3, whilst the difference in the CB positions of these semiconductors allows an electron cascade pathway from $BiVO_4$ to SnO_2 to WO_3 through to the counter electrode. Very recently Domen demonstrated that triple junction Co-Pi/$BiVO_4/WO_3$ nanorod photoanodes produce a photocurrent of *ca.* 3 mA/cm^2 at 1.23V *vs* RHE and 60% IPCE at 400 nm, again due to electron transfer to WO_3, but further enhanced *via* light trapping by WO_3 nanorods and hole transfer to Co-Pi for efficient water oxidation.[48] Furthermore, it has recently been reported that $BiVO_4/CuWO_4$ heterojunctions overcome the stability issues posed by WO_3 and can exhibit photocurrents as high as 2 mA/cm^2 at 1 V (*vs* Ag/AgCl).[59]

Recently, a $BiVO_4/WO_3$ "double-deck inverse opal junction" synthesised by swell-shrinking around polystyrene spheres exhibited a photocurrent density of *ca.*3.3 mA/cm^2 at 1.23 V *vs* RHE, enhancing the poor charge carrier mobility of $BiVO_4$ by combining it with a WO_3 skeleton and increasing the surface area through the inverse opal structure.[60] However, the most promising work involving $BiVO_4/WO_3$ junctions described a triple junction FeOOH-NiOOH/(W,Mo)-$BiVO_4/WO_3$ helix nanostructure that achieved a benchmark photocurrent of 5.35 mA/cm^2 at 1.23 V *vs* RHE and near unity IPCE at 420 nm, caused by a synergy between light trapping, enhanced charge separation and high surface area of the WO_3 helix.[49] Diffusion of tungsten from the WO_3 layer into $BiVO_4$ creates a gradient doping of W, beneficial for charge separation, and additionally could introduce a smoother interface between $BiVO_4$ and WO_3.

b) $BiVO_4$/ZnO

The use of ZnO as a highly mobile electron acceptor has seen its employment in a wide range of heterojunctions for water splitting, and its coupling with $BiVO_4$ has resulted in several mechanisms for enhanced activity. We have demonstrated that nanoparticulate $BiVO_4$/ZnO nanorod photoanodes exhibit high photocurrents under visible light irradiation (*ca.* 2 mA/cm^2 at 1.23V *vs* RHE) and the introduction of a Co-Pi surface oxygen evolution catalyst (OEC) improved the photocurrent to *ca.* 3 mA/cm^2 and IPCE to 47% at 410 nm (Figure 4a).[50] For this triple junction, the mechanism proposed by us allows for electron transfer from $BiVO_4$ to ZnO rods followed by hole transfer to Co-Pi as the flat-band position (E_{fb}) of $BiVO_4$ was found to be more negative than ZnO rods and hence provides a sufficient driving force. The efficiency was further improved due to the light trapping effect of vertically aligned ZnO rods (Figure 4).

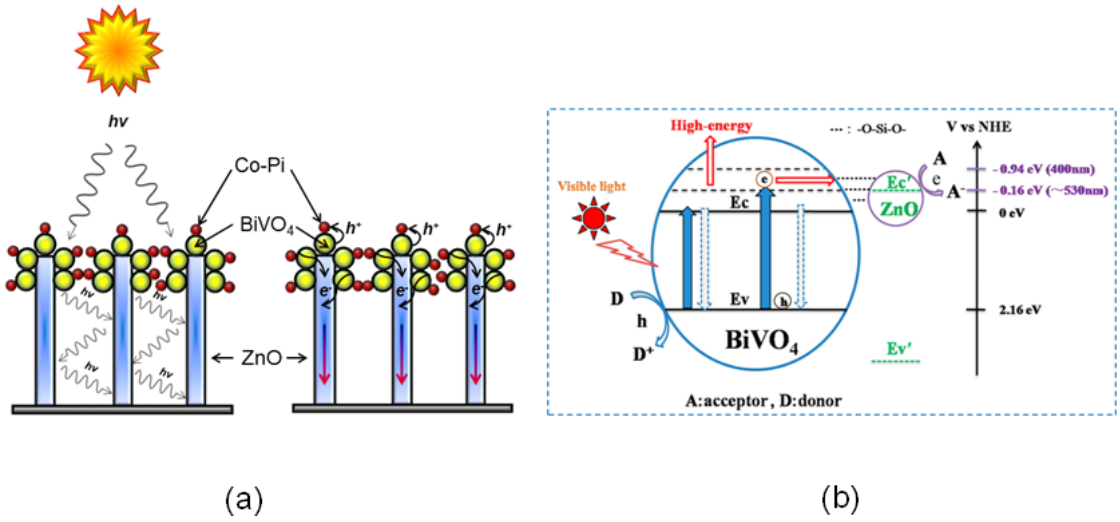

Figure 4: (a) Design strategy of a Co-Pi/$BiVO_4$/ZnO heterojunction by Moniz *et al.*,[50] involving 1) increased light absorption and charge generation in both $BiVO_4$ and ZnO in conjunction with light trapping effect of the nanorods, and 2) electron injection into ZnO nanorods followed by prompt electron transport along ZnO nanorods and 3) simultaneous hole transfer to Co-Pi for efficient water oxidation; (b) Charge transfer mechanism proposed by Fu *et al.*,[61] involving spatial transfer of visible light excited high-energy electrons from $BiVO_4$ to ZnO. Reprinted with permission from Ref. [61] Copyright (2014) American Chemical Society.

On the other hand, Fu *et al.*[61] recently suggested that the mechanism of charge transfer in $BiVO_4$/ZnO junctions is even more complex and unique. They suggest spatial transfer of visible-excited high-energy electrons from $BiVO_4$ to ZnO on the basis of EPR and photocurrent action spectra, whilst the

insertion of a silicate bridge improved charge transfer between the individual materials (Figure 4b). It was believed that the energy level of the high energy electrons is higher than that of the proton reduction potential for H_2 production from water. Thus, it is a very unusual electron transfer process with great significance for improving the efficiency of heterojunction photocatalysts. Reisner *et al.* have demonstrated another strategy; Al-doped ZnO inverse opals were introduced as a charge transporter in $BiVO_4$ photoanodes to improve charge collection; the $BiVO_4$/io-AZO heterostructure produced a photocurrent of 1.5 mA/cm^2 at 1.23V *vs* RHE, 3 times the activity of planar $BiVO_4$ photoanodes.[51]

$BiVO_4/TiO_2$

Comparatively less work has been reported on the activity of $BiVO_4/TiO_2$ junctions for water splitting, possibly due to the ambiguity of the conduction band alignment of $BiVO_4$. Nevertheless Fu *et al.*[62] observed that visible-light excited high energy electrons in $BiVO_4$ can transfer to the CB of TiO_2, prolonging their lifetimes and promoting charge separation, which was investigated using PEC measurements and surface photovoltage spectroscopy, similar to their report on $BiVO_4$/ZnO. However, our mechanism is intrinsically different - we have demonstrated that $BiVO_4/TiO_2$ junction composites formed by spin coating show a fourfold enhancement in activity for water oxidation compared to the bare materials due to improved charge transfer from $BiVO_4$ to TiO_2 and the unique ultrafine morphology of our materials.[63]

c) $BiVO_4$/carbon-based materials

There are few reports on the coupling of $BiVO_4$ with carbon-based materials (nanotubes, graphene) to enhance their activity for water splitting. Kudo *et al.*[64] reported the coupling of reduced graphene oxide (RGO) to $BiVO_4$ which yielded a near 10-fold enhancement in PEC activity compared with pure $BiVO_4$ under visible light illumination. This improvement was attributed to the longer electron lifetime of excited $BiVO_4$ as the electrons are injected to RGO instantly at the site of generation, leading to a significant reduction in charge recombination. Nevertheless, the total photocurrents (*ca.*

0.1 mA/cm^2 vs Ag/AgCl) and IPCE (4% at 400 nm) are much lower than the before mentioned $BiVO_4$/metal oxide junctions and suggest more work is needed to improve the overall activity of $BiVO_4$/carbon based junctions. However, most carbon-based materials are extremely cheap in comparison to most semiconductors and precious metals, and therefore if made more efficient could be considered a viable option.

3.2 Visible-light driven photocatalyst/OEC junctions

The efficient conversion of H_2O to H_2 and O_2 catalyzed by materials comprised of earth-abundant elements is of fundamental importance to solar-fuels devices. Integrated devices that couple light-capturing semiconductors with oxygen evolution catalysts (OECs) to efficiently split water show particular promise as a means of direct production of solar fuels. A large overpotential (η), which is the extra potential needed to be applied beyond the thermodynamically required value, is always mandatory for fuel production due to the relatively slow kinetics of the oxygen evolution reaction (OER).[65] An OEC functions through collection of photoholes from the light absorbing semiconductor, thus aiding charge separation, and also lowers the activation energy for water oxidation, which occurs solely on its surface. The OEC usually self-assembles on the light absorber and can be regenerated in-situ, some even at low pH.[66] The complicated mechanism of water oxidation on a typical OEC has been previously investigated.[67] Of the numerous earth-abundant electrocatalysts identified, the most promising for low-cost, efficient solar fuels synthesis contain cobalt, iron and nickel species.[68–70]

a) $BiVO_4$/OEC

The loading of oxygen evolution catalysts (OECs), such as cobalt phosphate (Co-Pi)[71,72,69] on $BiVO_4$ helps to improve the kinetics for water oxidation and suppresses the accumulation of holes at the photoanode/electrolyte interface which can often result in photocorrosion. It has been widely reported that $BiVO_4$ suffers from poor electron conductivity[73] coupled with poor kinetics for water oxidation and significant recombination in the bulk.[73] Co-Pi OEC prepared by photo-deposition onto $BiVO_4$ has been shown to exhibit superior performance for water oxidation and exhibit favourable cathodic shifts in onset potential,[52,74] because photo-deposition ensures the selective deposition of Co–Pi OEC

anywhere on the $BiVO_4$ surface where photogenerated holes are available, it results in a uniform coating of the Co–Pi OEC. $BiVO_4$ photoanodes with a *ca*. 30 nm Co-Pi OEC layer grown by Abdi *et al.*[54] exhibited photocurrents of ~1.7 mA/cm^2 at 1.23 V *vs* RHE, more than double that of bare $BiVO_4$. Similarly, Pilli *et al.* showed that the photocatalytic activity of Mo-doped $BiVO_4$ electrodes is enhanced by over two times with Co-Pi loading[52] and the activity of W:doped $BiVO_4$[75] and $SiO_2/BiVO_4$[76] photoanodes have resulted in similar enhancements after addition of Co-Pi. Similarly, FeOOH OEC has been coupled to $BiVO_4$ photoanodes and resulted in a near 10-fold enhancement in photocurrent together with a 500 mV cathodic shift in onset potential. Strikingly, the FeOOH layer significantly improved the stability of $BiVO_4$ during prolonged illumination.[55] Coupling both FeOOH and NiOOH as dual-layer OECs onto porous $BiVO_4$ electrodes has recently resulted in the report of photocurrents as high 2.73 mA/cm^2 at a potential as low as 0.6 V *vs* RHE, clearly representing one of the most encouraging results seen so far for $BiVO_4$.[56] This dual-layer OEC reduces interface recombination at the $BiVO_4$/OEC junction while creating a more favourable Helmholtz layer potential drop at the OEC/electrolyte junction. Nickel-borate (Ni-B) OEC has also been utilised with $BiVO_4$ photoanodes to enhance the photocurrent generation by a factor of 3–4 times, cathodically shift the onset potential and exhibit a near 3 fold improvement in IPCE.[57] Furthermore, we have recently demonstrated that this OEC has further functionality as an inert, earth abundant passivation layer for unstable photoelectrodes, resulting in over one hour stability compared with the poorer stability of less than twenty minutes exhibited by the bare photoelectrode.[77]

b) Fe_2O_3/OEC

The most successful junctions comprising α-Fe_2O_3 involve its coupling with surface OECs that can trap the photohole, provide effective charge carrier separation and improve the kinetics for water oxidation. Zhong *et al.*[78] electrodeposited Co-Pi onto α-Fe_2O_3 electrodes and observed a 350 mV cathodic shift in onset potential for water oxidation and a near two-fold increase in IPCE at 450 nm to ~20% at pH 13. The same group found that at pH 8, a more disperse, thinner 100 nm Co-Pi layer was able to significantly improve the photocurrent density by nearly five times and cathodically shift the onset by ~500 mV compared to α-Fe_2O_3 at 1 V vs RHE,[79] whilst further optimisation of the Co-Pi

deposition process yielded photocurrents approaching 3 mA/cm^2 at 1.23 V vs RHE.[80] Using TAS, it has been observed that Co-Pi suppresses the kinetics for electron-hole recombination by over three orders of magnitude and thus Co-Pi/ α-Fe_2O_3 electrodes require smaller anodic potentials for photocurrent generation,[81] whilst under applied bias, slower electron-hole recombination is assigned primarily to enhanced electron depletion in α-Fe_2O_3.[82] The use of photo-deposited Ni-B OEC on α-Fe_2O_3 nanorods resulted in ~200 mV cathodic shift of the onset potential to nearer its flat-band potential and a 9.5 fold enhancement in the photocurrent density at 0.86 V *vs.* RHE.[83]

c) WO_3/OEC

Choi *et al.*[84] deposited Co-Pi OEC on WO_3 photoanodes and found that not only did the onset potential shift cathodically toward the flat-band potential of WO_3, the photocurrent-to-O_2 conversion efficiency increased from ~61% for WO_3 to ~100% for Co-Pi/WO_3 and stability is greatly improved. Strikingly, for bare WO_3, it was found that 39% of photogenerated holes were used to form peroxo species on the surface, which led to gradual decomposition of the electrode. Likewise, in order to improve the activity and stability of WO_3 toward water oxidation, Wang *et al* deposited a Mn oxo-catalyst on ALD-grown WO_3 films and found that although the activity enhancement over bare WO_3 was not significant, the stability of the films improved remarkably over a wide pH range.[85]

3.3 Fe_2O_3-based junctions

In possessing a band-gap of ~2.1 eV, hematite (α-Fe_2O_3) has many potential advantages as a photoanode for PEC water splitting, namely, its absorption in the visible region, low-cost, abundance, non-toxicity and good stability.[86] It can theoretically produce water oxidation current densities of 12.6 mA/cm^2 under AM 1.5G illumination; however it suffers from high charge recombination in the bulk, low conductivity, poor kinetics for water oxidation at its surface and short hole diffusion lengths.[87,88] This is the reason why a relatively high external bias is required for water oxidation, making its use in a suspension system for water splitting unfeasible. A review of hematite-based photoanodes has recently been published and readers are directed to this for current progress in the field.[86]

Coupling α-Fe_2O_3 to other metal oxide semiconductors has seldom been reported, however Sivula *et al*[89] reported the use of a WO_3 host scaffold to improve light absorption and increase the surface area of α-Fe_2O_3. Higher activity for water oxidation was exhibited by the α-Fe_2O_3/WO_3 electrode because more α-Fe_2O_3 are closer to the hematite/electrolyte interface, allowing a greater fraction of the photo-generated holes to transfer to the semiconductor-liquid junction and participate in water oxidation. Feng *et al*.[90] have demonstrated the use of an α-Fe_2O_3 core as an electron acceptor in a α-Fe_2O_3 nanorod/graphene/$BiV_{1-x}Mo_xO_4$ core/shell heterojunction arrays for PEC water splitting (Figure 5). In the heterojunction, the energy bands of the Fe_2O_3 and $BiV_{1-x}Mo_xO_4$ shift upward and downward, respectively, followed by diffusion of carriers until the Fermi levels of Fe_2O_3–NA and $BiV_{1-x}Mo_xO_4$ reach equilibrium, resulting in current densities close to 2 mA/cm^2 at 1 V vs RHE, a near four-fold increase over bare α-Fe_2O_3.

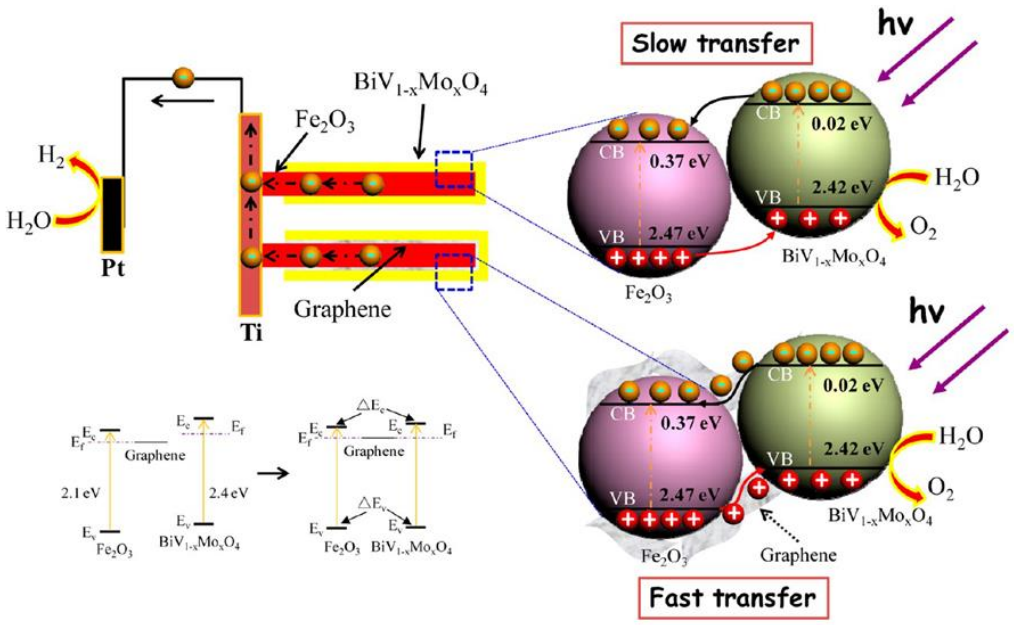

Figure 5: Band alignment and charge transfer in a Fe_2O_3 nanorod/graphene/$BiV_{1-x}Mo_xO_4$ core/shell heterojunction array. Reprinted with permission from Ref. [90]. Copyright (2012) American Chemical Society.

Three-dimensional cobalt-doped α-Fe_2O_3 nanorod arrays (Co-α-Fe_2O_3-NA)/$MgFe_2O_4$ heterojunction[91] produced a photocurrent of 3.34 mA/cm^2 at 1.4 V vs RHE, 2.7 and 2 times larger than those of Fe_2O_3-NA and Co-Fe_2O_3-NA respectively. $MgFe_2O_4$ has a similar band-gap (~2.0 eV) to α-Fe_2O_3 and possesses suitable band-edge positions that match well with hematite in the junction. Upon irradiation, electrons are promoted from the VBs of Co-Fe_2O_3-NA and $MgFe_2O_4$ to their CBs,

followed by electron transfer from $MgFe_2O_4$ to Co-Fe_2O_3. Meanwhile, holes in the valence band and impurity level of Co-Fe_2O_3 transfer to that of $MgFe_2O_4$ to oxidise water to O_2. Electrophoretic deposition of catalytic iridium oxide (IrO_2) nanoparticles onto haematite photoanodes resulted in a dramatic shift in the onset potential from +1.0 to +0.8 V vs RHE and an increase in the plateau photocurrent from 3.45 to 3.75 mA/cm^2 under 1 sun illumination.[92] However during repeated scans the adherence of IrO_2 began to diminish and the shift in onset is decreased until more IrO_2 is loaded. Utilising a similar strategy, NiO/α-$Ni(OH)_2$–hematite electrodes also displayed improved activity toward water oxidation, achieving photocurrents up to 16 mA/cm^2,[93] whilst a NiO/Fe_2O_3 p-n junction[94] was used to promote charge separation through the use of NiO as an efficient hole acceptor which reduced the overpotential for water oxidation. Furthermore, Ti-doped Fe_2O_3/SnO_2 junction photoelectrodes exhibited a two-fold increase in electron lifetime at 0.13 V compared to Ti:Fe_2O_3.[95] In a separate study, α-Fe_2O_3/$ZnFe_2O_4$ composite electrodes were grown through surface treatment of Fe_2O_3 with Zn^{2+} ions and exhibited enhanced photocurrents due to *in-situ* charge separation, caused by electron transfer from $ZnFe_2O_4$ to α-Fe_2O_3 and hole transfer in the opposite direction.[96] We have recently observed that coupling α-Fe_2O_3 nanoparticles onto TiO_2 results in enhanced water oxidation due to facile electron transfer from TiO_2, supported by DFT calculations which revealed a resultant increased surface reactivity on TiO_2.[97]

Coupling of α-Fe_2O_3 to graphene nanoplates (GNP) of 0.2 wt.% allowed for efficient water oxidation (2.5 mA/cm^2 at 0.75 V vs SCE) under visible light irradiation, the mechanism of which was attributed to efficient charge transfer at the semiconductor/electrolyte junction, a red shift in the absorption spectra of the Fe_2O_3–GNP compared to pristine α-Fe_2O_3, and improved conductivity of α-Fe_2O_3 due to the introduction of conductive graphene.[98] Indeed, the relatively simple, low-cost strategy of coupling Fe_2O_3 to carbon-based materials reveals great potential to increase the efficiency for water splitting applications. The coupling of α-Fe_2O_3 to other metals/metallic species is seldom reported, however the underlying goal of improving the conductivity and improving the transfer of the electron to the counter electrode have led to more work on using highly conductive, high surface area metallic species as charge collectors.[99] For example, Wang *et al*[100] synthesised a α-Fe_2O_3/$TiSi_2$

nanonet core-shell heterojunction for water splitting. The work functions predict ohmic contact between n-type Fe_2O_3 and metallic $TiSi_2$, which led to excellent performance for PEC water splitting compared to planar α-Fe_2O_3 - almost 50% IPCE at 400 nm. Likewise the introduction of Al-doped zinc oxide (AZO) into α-Fe_2O_3 to form a Fe_2O_3–AZO junction improved electron collection to the counter electrode whilst increasing the surface area of the photoanode, resulting in almost double IPCE at 400 nm. However, AZO was found to have poor stability under the experimental condition without the ALD-grown α-Fe_2O_3 layer.[101] Furthermore, by forming a simple p-n Fe_2O_3 homojunction *via* ALD, the onset of photocurrent was shifted by almost 200 mV compared to bare n-type Fe_2O_3,[102] whilst an Si/α-Fe_2O_3 dual-absorbing heterojunction exhibited an even lower onset potential of ~0.6 V vs RHE, representing a cathodic shift of approximately 400 mV, achieved in part, by the utilization of low-energy photons by the Si nanowires.[103]

3.4 Ag_3PO_4-based junctions

Since the pioneering work of Ye *et al*[104] on the discovery of extremely high photo-oxidation on a visible-light driven Ag_3PO_4 semiconductor photocatalyst, there have been many reports that have attempted to not only improve its activity but address its rather limited stability upon light irradiation. Recently an almost unity quantum yield at 400 nm was reported for tetrahedral faceted Ag_3PO_4 in a suspension system for water oxidation,[15] and thus Ag_3PO_4 remains the most promising photocatalyst for oxygen evolution under visible light irradiation. In order to improve its activity and improve its stability, numerous heterojunctions have been synthesised in order to efficiently remove the photoelectron and inhibit its facile reduction to Ag metal. Whilst most reports measure the photodegradation of organics,[105,106,107] recent reports have focussed on water splitting. For example, AgX/Ag_3PO_4 (X= Cl, I, Br) core–shell particles displayed up to a four-fold enhancement for PEC water oxidation compared to bare Ag_3PO_4 electrodes (in Na_2SO_4 electrolyte) although their stability was not significantly improved,[105] however Ag_3PO_4/Ag/AgBr/RGO composites exhibited not only improved photocurrent but also stability. The rationale was valence band lowering of Ag_3PO_4 caused by the addition of Ag/AgBr, in addition to a degree of charge delocalisation induced by the graphene support.[108] In other words, depletion of the conduction band of n-doped Ag_3PO_4 through intimate

contact with silver nanoparticles leading to (a) a longer lifetime of holes, and (b) a downward shift of the Ag_3PO_4 valence band due to a charge transfer cascade to Ag and then RGO, resulting in higher water oxidation activity. Coupling Ag_3PO_4 with multi-walled carbon nanotubes (MWCNTs) using an emulsion-based architecture permitted the storage and shuttling of electrons away from visible light-irradiated Ag_3PO_4 to alleviate its photocorrosion, and allowed for spatial separation of the photogenerated oxygen at the surface.[109] By far one of the most promising heterojunctions based on Ag_3PO_4 is the $Ag@Ag_3(PO_4)_{1-x}/ZnO$ core shell photoelectrodes synthesised by Lin *et al*.[110] By covering a Ag core with a 2 nm thick nanoshell of $Ag_3(PO_4)_{1-x}$ ($Ag@Ag_3(PO_4)_{1-x}$) onto ZnO nanorods, superior PEC water oxidation activity was observed with a maximum photocurrent of 3.1 mA/cm^2 at 0.6V *vs* Pt counter electrode and an IPCE of 60% at 400 nm (Figure 6). Although the mechanism of charge transfer is still unclear, the authors suggest that the enhanced activity is due to the surface plasmon resonance of Ag which results in an increase in the optical absorption and thus the rate of electron-hole formation in nearby $Ag_3(PO_4)_{1-x}/ZnO$ junction. Nevertheless, further work is needed to obtain a simpler strategy to form more efficient Ag_3PO_4 junctions that are stable under prolonged light irradiation that could be incorporated into a practical device for overall water splitting.

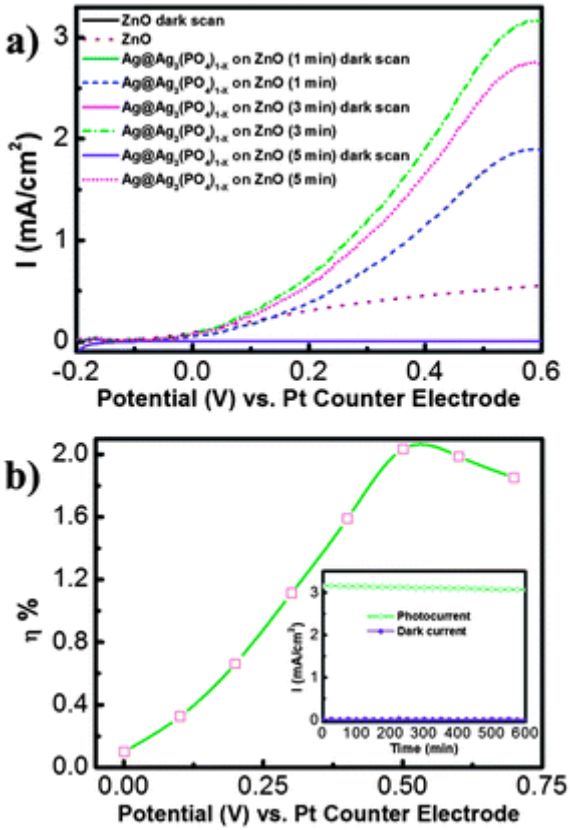

Figure 6: (a) I-V curves for $Ag@Ag_3(PO_4)_{1-x}$/ZnO core-shell photoelectrodes, (b) corresponding STH and I-T spectra (image from Lin *et al*).[110] Reproduced from Ref. [110] with permission from The Royal Society of Chemistry.

3.5 WO_3-based junctions

WO_3, akin to Fe_2O_3, has received considerable attention as a potential photoanode material for PEC water splitting as it possesses a band-gap in the visible range (2.4 eV), a long hole diffusion length (150 nm) compared to α-Fe_2O_3 (~4 nm) and has a VB position sufficiently more positive than the potential for water oxidation.[111] However, similar to haematite, the onset potential for water oxidation is relatively high (*ca.* 0.4 V) compared to other photoanodes. There are numerous reports of its use as an efficient electron collector when coupled to other semiconductors that have a more negative CB position, but relatively few reports of its use in junctions where WO_3 is the main light absorber. One of the main drawbacks of using WO_3 as a photoanode is its thermodynamic instability toward anodic photocorrosion and the formation of peroxo species on its surface that competes with O_2 production. Recently, the combination of a 5 nm ALD-deposited Al_2O_3 overlayer with WO_3 was shown to suppress the formation of surface peroxo-species through decreasing electron trapping whilst

promoting hole trapping, facilitating water photo-oxidation and retarding the recombination process.[112] The use of WO_3 coupled with RGO has been shown to increase the PEC activity for water splitting by lowering charge carrier recombination at the particle interface of WO_3, facilitated by the highly conductive RGO substrate.[113] A photocurrent of 1.1 mA/cm^2 at 1V vs Ag/AgCl was observed; however the onset potential (*ca*. 0.3 V vs Ag/AgCl) did not shift. Furthermore, electrochemical impedance spectroscopy (EIS) revealed that in the low bias region (0.4 V), the RGO does not improve charge separation; it is only at higher potentials (>1 V) that charge transfer is improved. Domen showed that PtO_x/WO_3 in a suspension system was able to readily evolve oxygen under visible light irradiation but the addition of small amounts of MnO_x, CoO_x, RuO_2 or IrO_2 as secondary cocatalysts resulted in better activity; evidenced by an apparent quantum yield of 14.4% at 420 nm with RuO_2.[114]

3.6 CdS-based Junctions

Different from an oxygen evolution photocatalyst $BiVO_4$, CdS is attractive due to its high efficiency for hydrogen evolution from water because it has a narrow band-gap (2.4 eV) and its conduction band is sufficiently more negative than the reduction potential of protons.[115] However, the issues of particle agglomeration, extremely poor stability in solution and high recombination rates of photogenerated electron–hole pairs severely limits its practical use for large-scale water splitting. Hence the synthesis of CdS-based junctions has been attempted to mitigate recombination, improve its surface area and more importantly, stabilize the material. Recent examples include the fabrication of Pt–PdS/CdS[116] which was shown to achieve a stable quantum efficiency of 93% for H_2 production in a suspension system and Ag_2S/CdS,[117] where holes in Ag_2S were used to oxidise sulphite ions which were used as a hole scavenger. CdS has been applied as a sensitizer onto TiO_2 nanotube arrays which resulted in improved PEC performance using a Na_2S scavenger due to facile electron transfer from the more negative CB of CdS into the CB of TiO_2,[118] and a similar mechanism was proposed for CdS/TiO_2/Pt photocatalysts.[119] CdS/ZnO/ZnO/CdSe nanowire arrays have also displayed much improved activity for PEC water cleavage where a photocurrent density of 12 mA/cm^2 at 0 V (vs Ag/AgCl) was reported (Figure 7).[120] In the reported CdS/CdSe/ZnO system, the Fermi levels of CdS, CdSe, and ZnO align so that the CBs of CdS and CdSe are close enough to allow electrons to

delocalize and transfer between the conduction bands. Although the electrons created in CdSe can be transferred to ZnO through the CdS layer, the presence of this intermediate layer increases recombination and limits electron collection efficiency. Having CdS and CdSe on the other side of ZnO alleviates this.

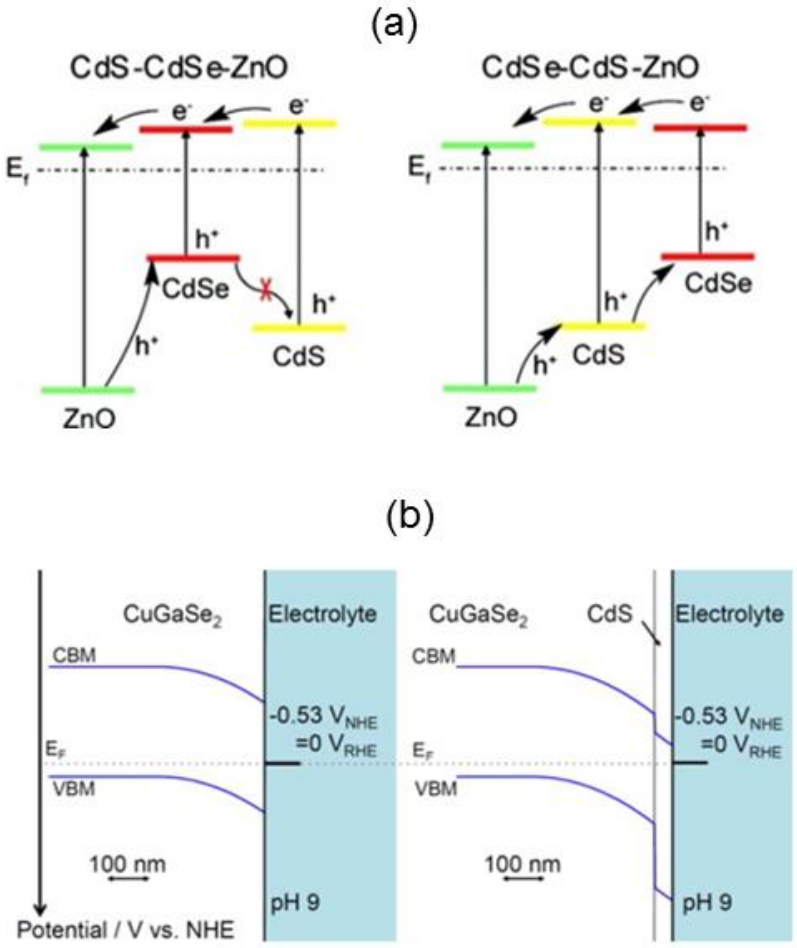

Figure 7: (a) Band alignment in CdS/CdSe/ZnO heterojunctions, from Wang *et al.*[120] Adapted with permission from Ref. [120]. Copyright (2010) American Chemical Society. (b) Calculated band alignment and bending at the solid−electrolyte interface for $CuGSe_2$ and CdS/$CuGSe_2$ electrodes, from Moriya *et al.* [121] Adapted with permission from Ref. [121]. Copyright (2013) American Chemical Society.

A thin layer of CdS on Pt/$CuGaSe_2$ forms a highly active p-n junction photocathode which was demonstrated to possess over 10 days stability for PEC water splitting and over 6 times the photocurrent of Pt/$CuGaSe_2$.[121] Here, CdS was reported to be only used as a visible light absorber as

$CuGaSe_2$ has a CB minimum of -0.8V and VB maximum of +0.9 V *vs* NHE, and thus could be utilised for H_2 evolution. The mechanism for the enhanced activity is associated with facile charge separation due to the p-n junction and increased thickness of the depletion layer at the solid-electrolyte interface. Furthermore, electron diffusion into CdS from $CuGaSe_2$ may occur due to the large VB maximum offset between the two materials (0.98V).

In a suspension system, a MoS_2 co-catalyst was loaded on CdS for photocatalytic H_2 production using lactic acid as a sacrificial agent under visible light.[122] The resultant H_2 evolution was found to be much higher than using Au or Pt as a co-catalyst which opened the path for using MoS_2 as a substitute for expensive noble metal H_2 catalysts, however the stability of the junction was not addressed. Similarly, WS_2 loaded CdS exhibited a high H_2 evolution rate of 420 μmol/hr/g under visible irradiation despite suffering from photocorrosion during testing, and although the photocathodic response of their WS_2/CdS electrode was better than bare CdS, it was much lower than the Pt/CdS electrode.[123] More recently, ZnO/ZnS/CdS/$CuInS_2$ core–shell nanowire arrays were reported to exhibit a photocurrent of 10.5 mA/cm^2 (in Na_2S/Na_2SO_3 electrolyte) and IPCE of 57.7% at 480 nm at 0 V versus Ag/AgCl.[124] The function of CdS was to enhance visible absorption and to form a p–n junction with $CuInS_2$, which would suppress recombination in $CuInS_2$.

Very recently the use of Au nanoparticles as a plasmonic sensitizer and charge facilitator in a CdS-Au-TiO_2 nanorod array junction resulted in a photocurrent of 4.07 mA/cm^2 at 0 V (vs Ag/AgCl) under full arc irradiation and a STH efficiency of 2.8% (Figure 8).[125] Using transient absorption spectroscopy (TAS), it was found that the junction allowed for an increase in the rate and number of transferred charge carriers, lower recombination and prolonged charge separation. With lower incident wavelength photons (λ<525 nm), photoelectrons are transferred from CdS through the Au particles to TiO_2, however an additional plasmonic energy transfer from the excited Au nanoparticles to TiO_2 via hot electrons excited by longer wavelength photons (525 nm – 725 nm) occurs, where CdS and TiO_2 are not excited (not a band transfer photo-excitation). This is clearly a unique mechanism and certainly offers much potential for increasing the efficiency of solar water splitting reactions.

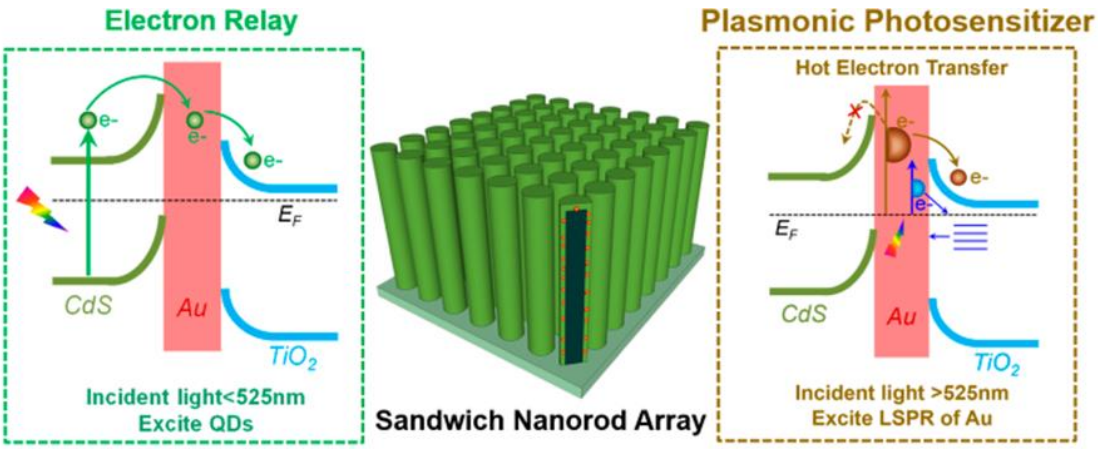

Figure 8: Role of Au nanoparticles in the electron relay effect of Au nanoparticles, facilitating the charge transfer from CdS QDs to TiO_2 nanorods under the irradiation of incident solar light with λ<525 nm, followed by hot electron transfer from Au particles into TiO_2 up to 725 nm excitation. Reprinted with permission from Ref. [125]. Copyright (2014) American Chemical Society.

CdS/Au nanorod arrays have displayed enhanced stability and photocathodic activity (*ca.* 4 mA/cm^2 at 0 V vs Ag/AgCl, Na_2S/Na_2SO_3 electrolyte) due to facile electron transfer to Au,[126] whilst conversely, it has been suggested that Au incorporation does not produce an enhancement in H_2 evolution compared to Pt.[127] Hence H_2 evolution rates of *ca.* 435 μmol/hr/g were exhibited by Pt NP decorated CdSe and CdSe/CdS NWs.[128] TAS measurements revealed that for a single junction, coating a semiconductor to form core/shell structures is beneficial since this increases carrier lifetimes by reducing the influence of surface defects which act as non-radiative recombination centres, whilst in the double junction, electron transfer from the shell to the metal occurs and in the case of Pt, results in a large increase in H_2 evolution. Furthermore the p-n junction NiS/CdS[129] exhibited an enhanced H_2 evolution and photocurrent due to improved charge transfer at the S-S interface induced by the junction. Coupling CdS to carbon-based materials such as reduced graphene oxide (RGO) or N-doped graphene also improves H_2 production under visible light irradiation.[130,131] Another unique charge transfer mechanism was reported by Xie *et al*. for their mesoporous CdS-ZnS core-shell particles for hydrogen evolution from water (729 μmol/h/g).[132] In terms of band alignment, the structure is a Type I heterojunction and under visible light both the photoexcited electrons and holes in the CdS core cannot transfer to the ZnS shell due to its higher CBE and lower VB position. However, it was

proposed that the presence of acceptor states within the band-gap (Figure 9), akin to the mechanism of charge transfer in DSSCs, allow for spatial transfer of holes from photo-excited CdS to the ZnS shell, promoting charge separation and higher photocatalytic activity.

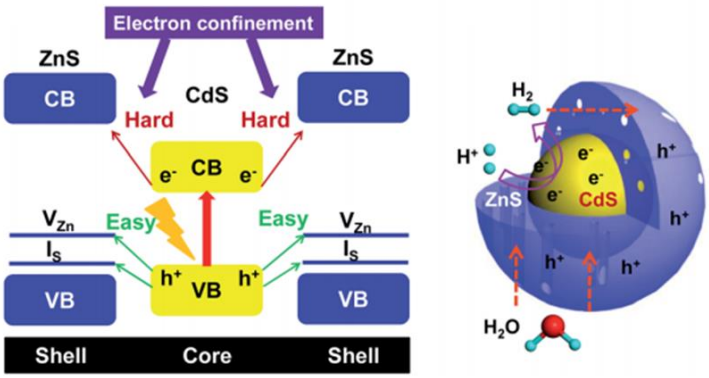

Figure 9: Band structure alignments of the CdS–ZnS core–shell structure and schematic of the photoexcited charge carrier distribution and related photocatalytic reactions. Reproduced from Ref. [132] with permission from The Royal Society of Chemistry.

3.7 C_3N_4 –based junctions

Graphitic (polymeric) carbon nitride (g-C_3N_4) is the most stable allotrope of carbon nitride and has attracted much attention in recent years for photocatalytic hydrogen evolution from water splitting in suspension systems after the breakthrough report by Antonietti *et al.*[133] It has the appropriate electronic structure with a band-gap in the visible region (2.7 eV) and a conduction band position sufficiently negative to drive the two electron proton reduction to hydrogen. When the efficient electron or hole scavenger is utilised, the catalyst can reduce or oxidise water with and without co-catalysts; very recently we reported g-C_3N_4 synthesised from urea which exhibited an hydrogen evolution rate (HER) of nearly 20 000 μmol/h/g under full arc irradiation and an internal quantum yield of 26.5 % under visible light (400 nm), a direct result of its more negative CB position and improved exciton distribution over its structure.[16] Numerous co-catalysts have been incorporated with g-C_3N_4 to achieve better performance, such as RuO_x, Rh, Ir, Pt, Au, Pd, as well as through doping with fluorine and sulphur.[134] Several heterojunctions incorporating C_3N_4 have been reported for water splitting, for example g-C_3N_4–$SrTiO_3$:Rh evolved 223.3 μmol h^{-1} of H_2 under visible irradiation, over three times that of $SrTiO_2$:Rh.[135] Carbon-based electron acceptors also facilitate more efficient charge

separation,[136] for example, g-C_3N_4/graphene composites exhibited a 3 fold enhancement in photocurrent and H_2 production under visible light compared to bare g-C_3N_4.[137] Photoluminescence (PL) measurements confirmed quenching of luminescence in the junction so the apparent mechanism for the enhancement was due to the ability of graphene sheets to act as conductive channels to efficiently separate the photogenerated charge carriers, while a similar mechanism was proposed in a red phosphorus/C_3N_4 junction.[138] As a visible light absorber, C_3N_4 has been coupled to many wide-band gap semiconductors to improve solar harvesting. A 50 wt.% C_3N_4/TiO_2 junction was found to double H_2 evolution compared to pure C_3N_4 under visible irradiation.[139] Since the CB edge of g-C_3N_4 (−1.12 eV) is more negative than that of TiO_2 (−0.29 eV) the photoinduced electrons on g-C_3N_4 transfer easily to TiO_2 before recombination.[140] Furthermore, g-C_3N_4 coated $SrTiO_3$ also displayed a high HER of 440 μmol h^{-1} g^{-1} under visible irradiation as a result of electron transfer from the CB of C_3N_4 to that of $SrTiO_3$ followed by migration to the Pt co-catalyst.[141] A ZnO photocatalyst hybridized with graphite-like C_3N_4 *via* a monolayer-dispersed method exhibited a fivefold increase in photocurrent under UV irradiation and visible light driven photocurrent, along with suppression of ZnO photocorrosion.[142] The enhancement under UV irradiation was due to the high separation efficiency of photoinduced holes from ZnO to the HOMO of C_3N_4, whilst under visible light irradiation, the electron excited from the HOMO to the LUMO of C_3N_4 may directly inject into the CB of ZnO. 1.1% NiS/C_3N_4 composites have also shown to have appreciable activity for H_2 production from water,[143,144] whilst similarly, the use of NiS_2 as a co-catalyst for H_2 production on C_3N_4 has recently been reported.[145] The coupling of high surface area C_3N_4 with Ta_3N_5 also resulted in enhanced visible light driven H_2 evolution[146] and g-C_3N_4-CdS QDs composites improved the hydrogen production over bare g-C_3N_4 by over 9 times due to *in-situ* electron transfer to CdS, however the photocurrent recorded was actually quite small,[147] with a similar mechanism reported for C_3N_4/CdS core-shell nanowires.[148] In general, research on C_3N_4-based junctions has concentrated on H_2 evolution from suspensions systems as the O_2 evolution and photoanodic PEC activity is still moderate,[149] hence recent work in this field has sought to improve the photocurrent obtainable from C_3N_4 using junction structures if suitable electrodes can be synthesised. Examples include a C_3N_4 nanosheet/N-doped graphene/layered MoS_2 triple junction,[150] where electron transfer from C_3N_4

via highly conductive graphene to MoS_2 improves the photoresponse, and more recently, a 3D branched $CoO_x/C_3N_4/WO_3$ junction which exhibited the highest anodic photocurrent for a C_3N_4-based electrode (*ca.* 1.5 mA/cm^2 at 1.23V vs RHE).[151] This architecture utilised WO_3 as an electron acceptor and CoO_x as a surface oxidation catalyst, thus proving that a high anodic photocurrent from a C_3N_4 absorber is achievable (Figure 7). When the heterojunction is formed, the space charge layer creates a built-in electric field, which separates the electrons and holes upon illumination.

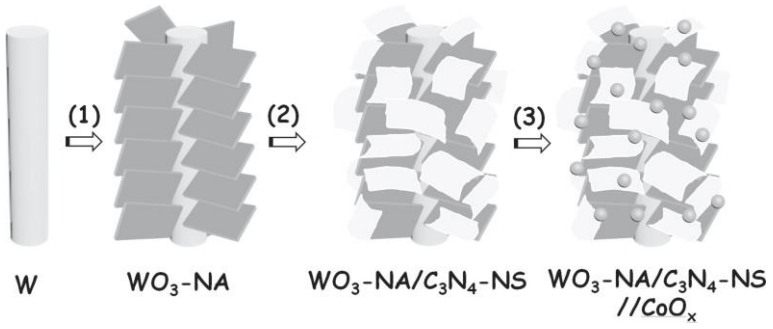

Figure 7: Construction of a 3D branched $CoO_x/C_3N_4/WO_3$ heterojunction photoelectrode, image taken from from Hou *et al.*[151] Copyright 2014 Wiley-VCH Verlag GmbH & Co. KGaA, Weinheim.

3.8 Cu_2O-based junctions

Cuprous oxide (Cu_2O), a p-type semiconductor with a direct band-gap of ~2 eV, is another visible-light responsive candidate with a theoretical maximum photocurrent of ~-15 mA/cm^2 and 18% STH efficiency under AM 1.5 light. Within the last ten years, much research has been undertaken in order to take advantage of the comparatively negative CB position of Cu_2O for photoelectrochemical hydrogen production from water. One of the main limiting factors in the use of Cu_2O is its poor stability because the redox potentials for the reduction and oxidation of monovalent copper oxide lie within the band-gap. To address these issues, Graetzel *et al* reported a $Cu_2O/ZnO/Al_2O_3/TiO_2$/Pt electrode (Figure 8a) capable of photocurrents as high as -7.6 mA/cm^2 at 0 V *vs* RHE with improved stability due to the protective nature of TiO_2 and high conductivity of ZnO/Al_2O_3 (AZO).[152] This work has catalysed further research into junctions that can not only protect Cu_2O, but enhance its activity. The same group reported a Cu_2O/n-AZO/TiO_2/MoS_{2+x} heterojunction photocathode that

exhibited improved stability in harsh acidic environments, returning a performance of -5.7 mA/cm^2 at 0 V *vs* RHE at pH 1.0.[153] Figure 10 shows the schematic relative band position for the Cu_2O/AZO/TiO_2/MoS_{2+x} photocathode after equilibration in the dark, assuming band edge pinning at the interfaces and taking the built-in potentials at the interfaces equal to the difference in Fermi levels. Electrons cannot flow from TiO_2 to Cu_2O due to the high potential energy barrier at the n-AZO/p-Cu_2O interface. UV photons drive the photo-deposition of MoS_{2-x} HER onto the TiO_2 surface, and photoelectrons can travel from the overlayers through to the Cu_2O VB at higher applied potentials.

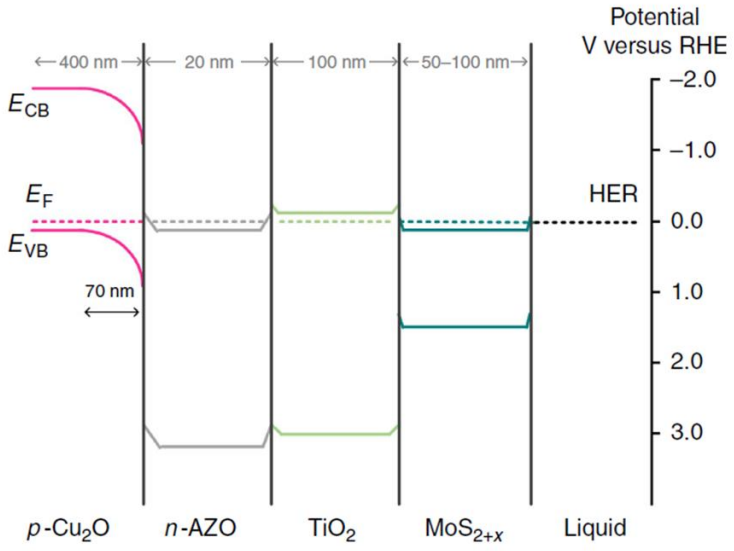

Figure 10: Band energy positions for the Cu_2O/AZO/TiO_2/MoS_{2+x} photocathode biased at 0 V vs RHE in the dark, assuming pinning of the band edges of the semiconductor at the interfaces. Figure taken from reference [153]. Reprinted by permission from Macmillan Publishers Ltd: Nature Communications, Ref. [153] copyright (2014).

Very recently the coupling of a surface protected Cu_2O with a MoS_2 HER catalyst and a Ni–Mo catalyst layer resulted in the highest reported photocurrent for a Cu_2O-based photocathode, at -6.3 mA/cm^2 at 0V vs RHE in 1M KOH electrolyte.[154] This appears to be the first report of the stability of MoS_2 in highly basic conditions, thus demonstrating significant potential to replace platinum as a cost-effective HER catalyst. Coupling of Cu_2O to n-type WO_3 is a strategy utilised to improve stability; for example, a Cu_2O nanowire photocathode modified with a thin film of NiO_x coupled to a WO_3 nanosheet photoanode exhibited a photocurrent density of −4.98 mA/cm^2 at −0.33 V *vs.* NHE and good stability over 20 min illumination time,[155] whilst a WO_3/Cu_2O NW also exhibited improved

photocurrent for water reduction.[156] Similarly, a Cu/Cu_2O/CuO composite electrode also exhibited improved activity[157] whilst Cu_2O/TiO_2 NW p-n junction exhibited a high photocurrent of 4 mA/cm^2 at 1 V *vs* SCE in Na_2SO_4 electrolyte and were highly active under visible light for RhB dye degradation[158] due to facile electron injection from Cu_2O into TiO_2.[159] Cu_2O, protected by an ultrathin carbon sheath, was coupled to TaON nanorods to yield a p-Cu_2O/n-TaON junction *photoanode*, which was shown to exhibit an IPCE of 59% at 400 nm, a photocurrent of 3.06 mA/cm^2 under 1 sun illumination at 1.0 V *vs* RHE and retained *ca.*87% of the initial activity after 60 mins irradiation.[39] The mechanism for the enhancement was attributed to the fast transfer of photogenerated electrons from Cu_2O to TaON together coupled with the high conductivity and protection from the electrolyte by the carbon sheath.

In a suspension system, we have demonstrated that Cu_2O can actively photoreduce protons to H_2 under visible light irradiation, however the stability was found to be a major limiting factor over its efficiency, but the coupling of Cu_2O to RuO_x was found to be more beneficial for CO_2 photoreduction to CO under similar conditions and exhibited a remarkable enhancement in stability.[160] TAS measurements confirmed that deposition of RuO_x nanoparticles on Cu_2O results in a two-fold increased yield of long-lived electrons, indicating partially reduced electron–hole recombination losses, and correlates with an approximately six-fold increase in the yield of CO_2 reduction to CO.[161] Likewise, we have demonstrated that the coupling of Cu_2O to RGO dramatically increases Cu_2O activity for CO_2 photoreduction and the photocurrent of the junction is nearly double that of the bare Cu_2O photocathode (Figure 11b). The improved activity together with the enhanced stability of Cu_2O was attributed to the efficient charge separation and transfer to RGO as well as the protection function of RGO,[162] whilst Tran *et al* also observed electron collection by RGO and enhanced stability when coupled to Cu_2O for photocatalytic hydrogen production.[163] Very recently an unusual mechanism was proposed for enhancement in activity and stability for CO_2 photoreduction by a Cu_2O/carbon quantum dot heterojunction.[164] Photogenerated holes in Cu_2O transfer to the surface of the CQDs for water oxidation, however an additional photoexcitation mechanism in the CQDs followed by electron transfer to Cu_2O was put forward. Therefore these examples represent promising solutions in

addressing the problem of inherent poor stability in Cu_2O-based water splitting photocatalysts, however more work is required to understand the charge transfer mechanisms involved. The relationship between the active components in $CuO/Cu_2O/TiO_2$ heterojunctions was realised by Wang *et al*.[165] Surprisingly, their $CuO\text{-}TiO_2$ does not initially catalyse the reduction of water, but instead undergoes a continuous in-situ restructuring process of reduction to Cu_2O. A $CuO/Cu_2O/TiO_2$ triple junction was observed *via* TEM, which evolves H_2 faster than P25 TiO_2 under solar irradiation. Hence their study reveals that Cu_2O is the active component in these specific junctions, yet is more suited to an in-situ restructuring process to inhibit post-synthesis oxidation.

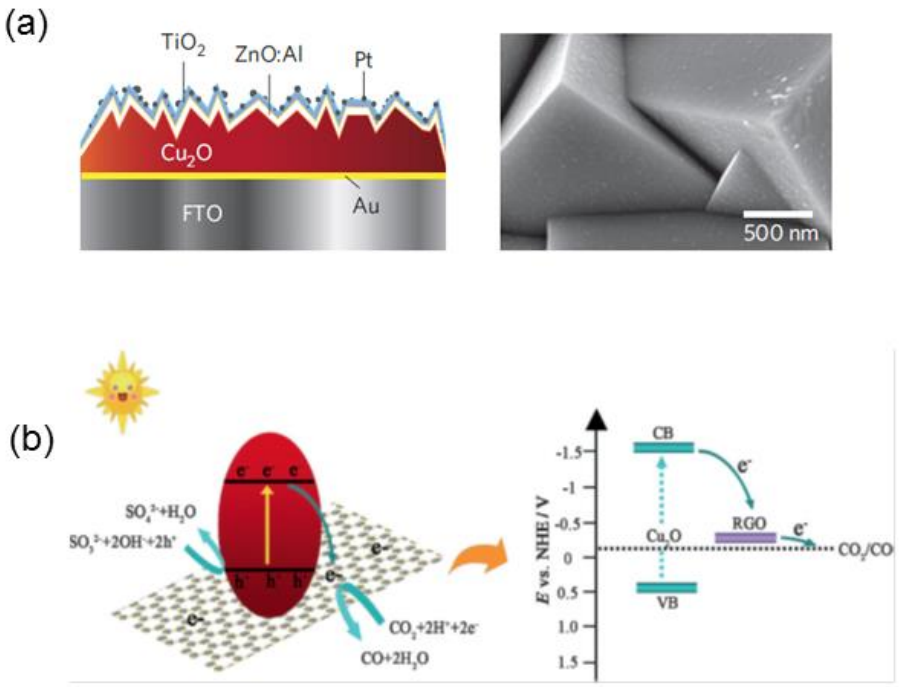

Figure 11: (a) Surface passivation and improved charge transfer in a Cu_2O photocathode using (a) TiO_2 and Al-doped ZnO, Adapted by permission from Ref. [152] Macmillan Publishers Ltd: Nature Materials, copyright 2011. (b) Charge transfer in Cu_2O/RGO, taken from Ref. [162] Copyright the authors, 2014 Wiley-VCH Verlag GmbH & Co. KGaA, Weinheim.

4. Observation of charge carrier kinetics in heterojunction structure

4.1 TAS

As stated in the introduction, the moderate efficiencies of semiconductor water splitting are, more often than not, due to non-radiative electron–hole recombination, occurring prior to the surface reactions of electron and holes with water. As carrier lifetimes are on the order of femtoseconds to nanoseconds, to as much as seconds after light absorption, a frequently used method to measure their decay kinetics is transient absorption spectroscopy (TAS). It is a technique most commonly used to measure kinetics of charge carriers in solar cell materials, but its use has been demonstrated for PEC materials. The setup of the experiment has already been reviewed elsewhere,[166] but in brief, it is comprised of a laser that can emit light pulses of femtosecond duration, together with a lock-in amplifier and a device to measure the absorption spectra as a function of time, wavelength or applied bias. By using the appropriate scavenger, either the electron or hole transient decay can be measured. Barera *et al*.[166] describe the process by which a fraction (0.1-10%) of the molecules are promoted to an electronically excited state by an excitation (or pump) pulse. A weak probe pulse (i.e., a pulse that has such a low intensity that multiphoton/multistep processes are avoided during probing) is sent through the sample with a delay τ with respect to the pump pulse. The absorption spectrum of the excited sample minus the absorption spectrum of the sample in the ground state (ΔA) allows for calculation of the difference absorption spectrum. By varying the time delay (τ) between the pump and the probe and recording a ΔA spectrum at each time delay, a ΔA profile as a function of τ and wavelength λ, $\Delta A(\lambda,\tau)$, is obtained. This is consequently very useful for researchers in the field of solar fuels because in the case of heterojunction systems, supressing recombination and increasing carrier lifetimes are the main objectives.

Using the example of nanocrystalline TiO_2 (nc-TiO_2), it was found that the carrier lifetime strongly depended on the pulse intensity and that water oxidation occurs on the timescale of seconds, whereas recombination takes place on the order of microseconds.[8] Going further and looking at N-doped TiO_2 under visible excitation, its lack of activity for water oxidation was assigned to the rapid decay of visible light generated photoholes, which occurs on a much faster time scale than that required for water oxidation compared to nc-TiO_2.[167] Other visible driven photoanodes have been studied using this method by Pendlebury *et al*, who revealed that for α-Fe_2O_3 electrodes the amplitude of the long

lived hole signal is only ~10% of the initial hole signal, indicating that even under positive applied bias the majority of photogenerated holes still undergo rapid electron–hole recombination on the microsecond timescale.[168] This was followed by the observation that recombination in α-Fe_2O_3, not surface kinetics, is the major limiting factor for water oxidation.[87] As expected, surface modification with Co-Pi resulted in the observation of a cathodic shift in photocurrent and the appearance of long-lived hematite photoholes,[81,82] due to suppression of electron/hole recombination (Figure 12a). The presence of surface catalysts led to a decrease in the width of the space charge layer and Fermi level pinning, thus enhancing the size of the electron depletion layer.

For visible light active Cu_2O photocathodes, the introduction of RuO_x particles at the surface resulted in a significant increase in the yield of long-lived (>100 μs) Cu_2O electrons measured using TAS (Figure 12b), attributed to a reduction in fast electron–hole recombination losses due to hole transfer from Cu_2O to RuO_x, thereby increasing the spatial separation of electrons and holes and facilitating the photooxidation reaction by holes.[161]

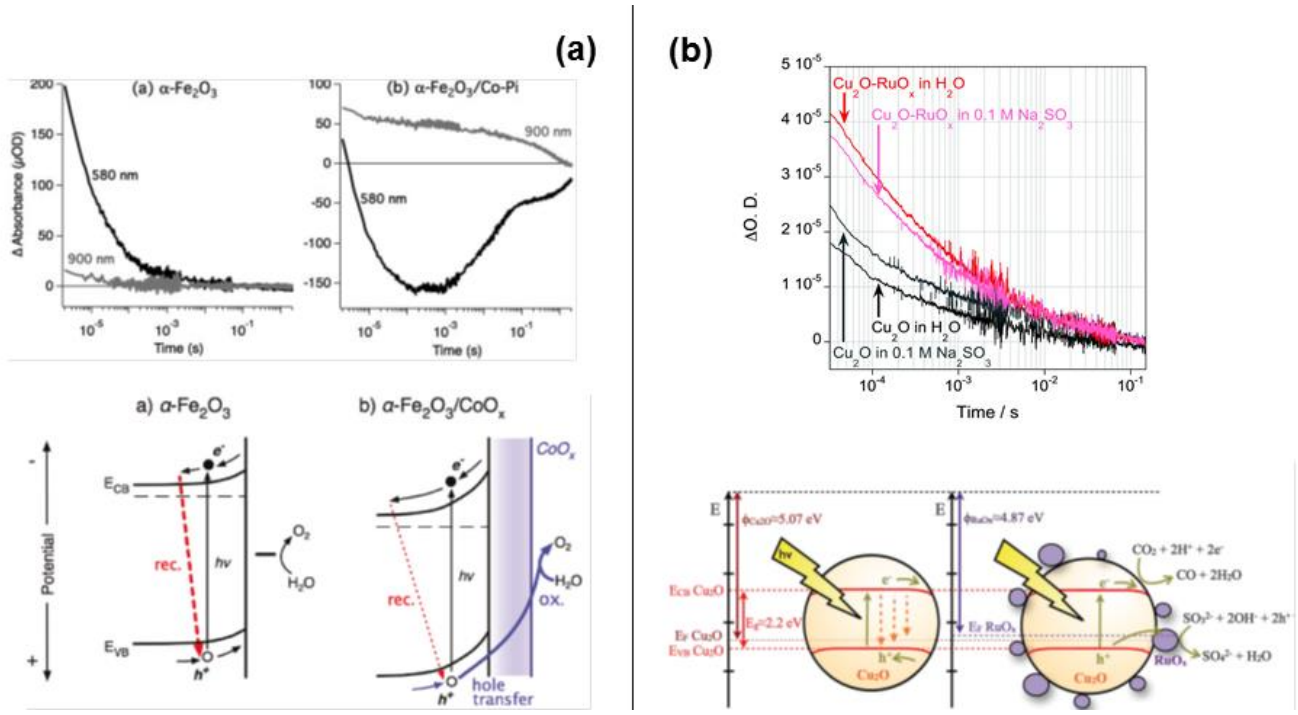

Figure 12: TAS spectra, band alignment and charge transfer mechanism in (a) Co-Pi/Fe_2O_3, and (b) Cu_2O/RuO_x, indicating long-lived hole (580 nm) and electron populations respectively. Reproduced from Refs. [81] and [161] with permission from The Royal Society of Chemistry.

In the case of $BiVO_4$, Ma *et al.*[169] have very recently reported that the yield of long-lived (0.1–1 s) photogenerated holes is observed to correlate as a function of applied electrical bias, assigned to kinetic competition between water oxidation and recombination of these surface accumulated holes with bulk electrons across the space charge layer. Crucially, two mechanisms were found to limit photocurrent generation in $BiVO_4$ photoanodes: firstly, rapid (≤ μs) electron-hole recombination, and secondly, recombination of surface-accumulated holes with bulk $BiVO_4$ electrons. For WO_3, Cowan *et al.* noted that rapid (<μs) electron/hole recombination dominates in the absence of an electron scavenger and that the production of long-lived holes with a lifetime in the milliseconds to seconds time scale is required for water oxidation to occur.[170] However it is clear from the literature that more junction architectures should be investigated using this technique, which could prove beneficial in providing experimental evidence of charge kinetics.

4.2 EIS

In addition to TAS, other techniques that can probe charge transfer kinetics and recombination include electrochemical impedance spectroscopy (EIS), photoluminescence spectroscopy (PL) and surface photovoltage spectroscopy. As PL spectroscopy depends on radiative recombination, which is generally considered a minority process, it will not be discussed in further detail in this review.

The basis of the electrochemical impedance spectroscopy (EIS) experiment is to apply a small amplitude sinusoidal ac voltage, $V(t)$, and then measure the amplitude and phase angle (relative to the applied voltage) of the resulting current, $I(t)$.[171] The impedance (Z), can then be calculated from Ohm's Law [Z = V(t)/I(t)]. Competition between the overall rates of hole transfer and recombination determines the fraction of the hole current j_h that is measured in the external circuit in EIS (Figure 13b).

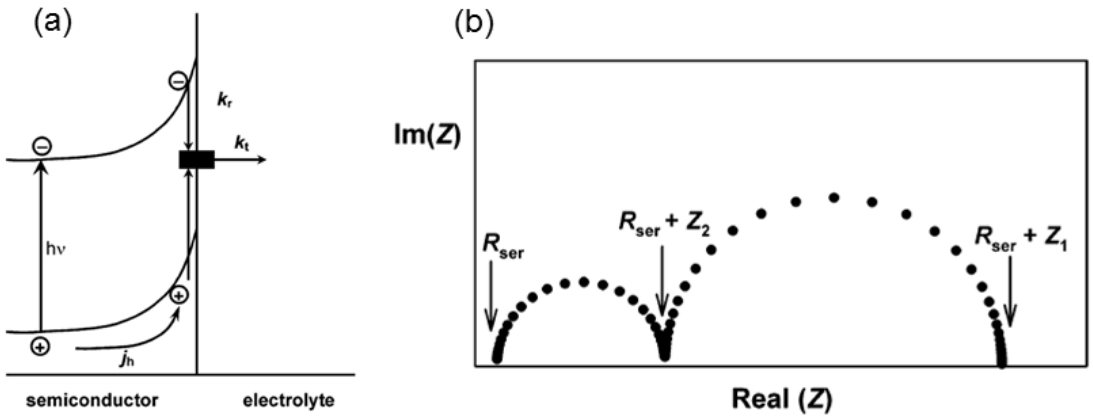

Figure 13: (a) Phenomenological kinetic scheme for PEIS analysis, (b) typical Nyquist plot showing the origin of Z_1 and Z_2, adapted from Ref. [172] with permission from The Royal Society of Chemistry.

The rate constants k_t and k_r (s^{-1}) in the equations for the EIS response are used to express the rates of hole transfer and recombination ($cm^{-2}\ s^{-1}$) in terms of the surface concentration of 'trapped holes.' It follows that k_r should depend on band bending $q\Delta\Phi$, because the electron concentration at the surface is given by:

$$n_{x=0} = n_{bulk} exp\left(\frac{-q\Delta\Phi}{k_B T}\right)$$

Where n_{bulk} is determined by the doping density.

Where the Helmholtz capacitance is larger than the space charge capacitance, the impedance Z_1 of the illuminated electrode (low frequency semicircle) is:

$$Z_1 = R_{ser} + \{k_t + k_r)/\left(\frac{q}{k_B T}\right) j_h k_r\}(1 + k_r/k_t)\}$$

It then follows that the high frequency limit of the low frequency semicircle, Z_2 is given by:

$$Z_2 = R_{ser} + \{k_t + k_r)/\alpha\left(\frac{q}{k_B T}\right) j_h k_r\}$$

The radial frequency ω_{max} (HF) corresponding to the maximum imaginary component of the high frequency semicircle is given by:

$$\omega_{max} = \left(\frac{1}{C_{sc}(Z_2 - R_{ser})]}\right)$$

Here R_{ser} is the series resistance, C_{sc} is the space charge capacitance, j_h is the current density corresponding to the flux of holes reaching the interface. The rate constants k_t and k_r are the first order rate constants for interfacial transfer and recombination respectively. The equation for Z_1 predicts the semicircles observed in Figure 13b.

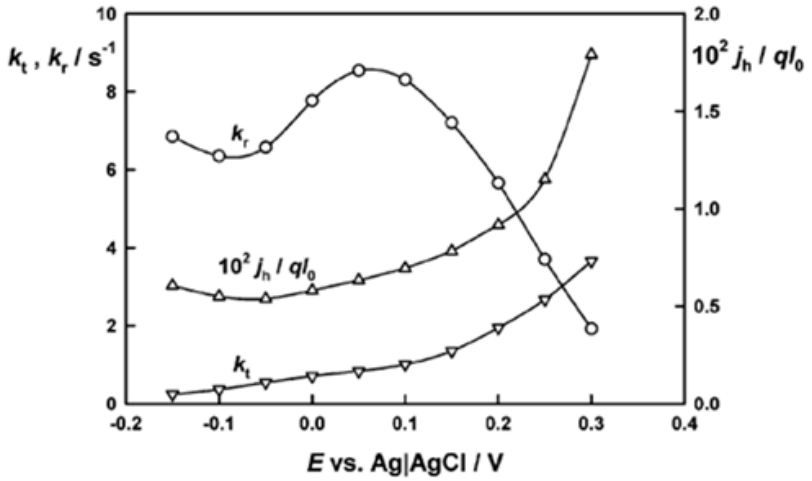

Figure 14: PEIS spectra of an α-Fe_2O_3 electrode, fitted and analyzed to obtain k_t, k_r, C_{sc} and j_h as a function of potential at a light intensity of 1.1 mW/cm^2. Reproduced from Ref. [172] with permission from The Royal Society of Chemistry.

From Figure 14, simplistically we can see that as the applied potential increases, the rate of recombination decreases (due to band bending) and charge transfer increases. Thus when the EIS is fitted using the appropriate equivalent circuit model, the resultant impedance semicircle (Nyquist plot) gives some indication as to the efficiency of charge transfer between the semiconductor and electrolyte when the value of the charge transfer resistance at the interface is computed. J_h is likely to be lower than the product of qI_0 (I_0 is the photon flux) because electron–hole pairs generated outside the space charge region are mostly lost through recombination. Recently, this technique has been successfully applied to bulk heterojunction solar cells based on the determination of chemical

capacitance and recombination resistance.[173] Modern potentiostats are able to measure electrical impedance spectroscopy at a variety of frequencies and will construct the Nyquist plot; the fitting of the equivalent circuit to an in-built model or to such developed by the user is a common function of the accompanying software. There are many examples of its use in when applied to junction architectures such as $BiVO_4/WO_3$, (Figure 10)[46] CdS/WO_3,[174] Cu_2O/RGO[162] and g-C_3N_4/ZnO[175] to explain charge transfer and decreased resistance.

Furthermore, in the equivalent Randle circuit, values of R_{ct} may be compared (where R_s is the solution resistance, Q_1 is the constant phase element (CPE) for the electrolyte/electrode interface, and R_{ct} is the charge transfer resistance across the interface of electrode/electrolyte interface). Thus, a comparatively lower value of R_{ct} is expected for a heterojunction which exhibits favourable charge transfer characteristics. Lee *et al.*[46] observed a significantly decreased value for R_{ct} in their optimised $BiVO_4/WO_3$ junction (780 Ω) compared to bare $BiVO_4$ (8803 Ω , see Figure 15). Although one cannot obtain the rate constants via this interpretation, it assumes pure charge transfer control and no diffusion limitations or competing processes. Furthermore, the presence of defects and multi-layers is likely to yield different resistivities and requires a more complex model, so care must be taken when fitting the equivalent circuit. Nevertheless, this technique can provide information about the phenomenological rate constants describing the competition between charge transfer and recombination during water oxidation.

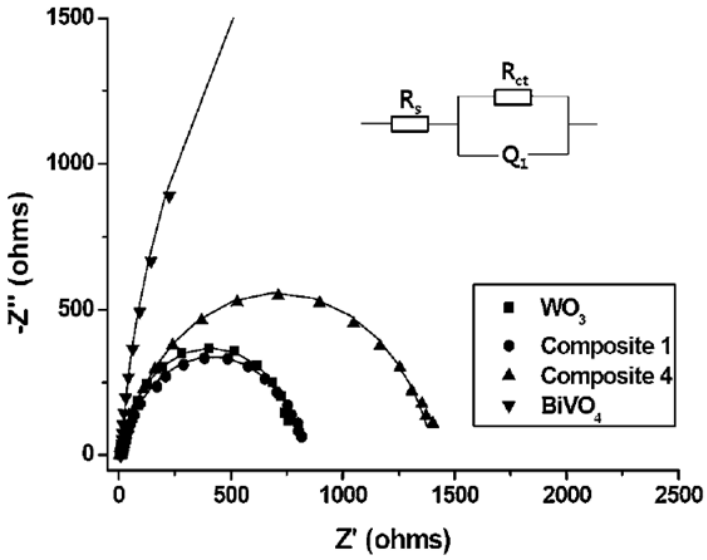

Figure 15: EIS spectra of the $BiVO_4/WO_3$ heterojunction proposed by Lee *et al* for improved PEC water splitting.[46] reproduced from Ref. [46] with permission from The Royal Society of Chemistry.

4.3 Surface photovoltage spectroscopy

Surface photovoltage spectroscopy has been used for many years to probe charge carrier kinetics and recombination in dye sensitized solar cells, and this measurement technique has only recently been applied to the field of semiconductor photoelectrodes for water splitting.[176] The surface photovoltage (SPV) is defined as the illumination-induced change in the surface potential; this non-destructive technique measures changes in band bending at the free semiconductor surface as a function of external illumination and can provide the researcher interested in heterojunction photocatalysis a wealth of qualitative and quantitative information. This includes, but is not limited to, the relative locations of the band positions, the degree of band-bending, defect states, surface dipole, diffusion lengths, recombination rates and flat-band potentials.

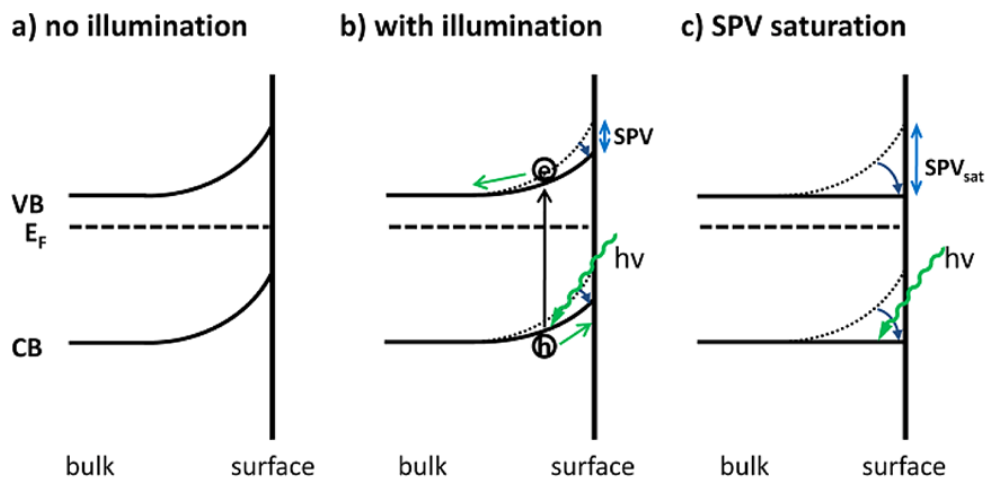

Figure 16: Schematic diagrams of the surface photovoltage effect, taken from Reference [177]. In figure (a), we observe upward band bending in a typical n-type semiconductor surface; in figure (b), the absorbed photons produce free charge carriers resulting in a partial band flattening; and in figure (c) the largest SPV saturation occurs to completely flatten bands. Copyright © 2010 WILEY-VCH Verlag GmbH & Co. KGaA, Weinheim.

For a detailed description of the experimental setup, readers are directed to a recent comprehensive review.[178] The set-up includes a light source, sample chamber containing a Kelvin Probe enclosed within a Faraday cage, chopper, lock-in amplifier and monochromator. The Kelvin Probe can be used to measure the contact potential difference (CPD), which is the difference between the work function of the metal tip of the probe and the semiconductor surface. On illumination, the probe measures the change in CPD. The absorbed photons induce the formation of free carriers by creating electron-hole pairs *via* interband transitions and/or release captured carriers via trap-to-band transitions, resulting in a significant amount of charge transferring from the surface to the bulk (or vice versa) and/or redistributed within the surface or the bulk. Since the electric potential and the charge distribution are inter-dependent, the potential drop across the surface space charge region, and surface potential change. It is important to note that the formation of a SPV occurs only if carrier generation is followed by net charge redistribution; the SPV response is positive for n-type materials and negative for p-type due to the different signs of the equilibrium surface potential. For a semiconductor with upward bent bands, irradiation will cause the band to flatten as the negative surface charge decreases as a result of hole transport to the surface (Figure 16); with the opposite occurring in semiconductors with downward bent bands, causing downward band bending to decrease. For increasing photon flux,

the energy bands may be completely flattened and the saturated SPV value is equivalent to the initial magnitude of band bending of the semiconductor.[23] Readers are directed to the comprehensive overview by Kronik for details of the experiment.[179]

Photovoltage (in volts or similar units) is measured as a steady state (SS; function of light wavelength) or as a transient measurement (TS; as a function of time). There are many examples of SPV used to determine the charge separation efficiency in heterojunction photoelectrodes. For example, Fu *et al*[62] used TS-SPV and SS-SPS to probe charge carriers in $BiVO_4/TiO_2$ composites (Figure 17). Coupling 5% TiO_2 to $BiVO_4$ resulted in a large increase in the SS-SPV trace, indicating better charge separation, and the TS-SPV signal revealed a much longer carrier lifetime of ~3 milliseconds. This was attributed to the unusual spatial transfer of visible-light-excited high-energy electrons of $BiVO_4$ to TiO_2, however the overall photocurrent recorded for their optimised composite electrode was only ~0.3 mA/cm^2 at 0.5 V *vs* Ag/AgCl (1M NaOH electrolyte).

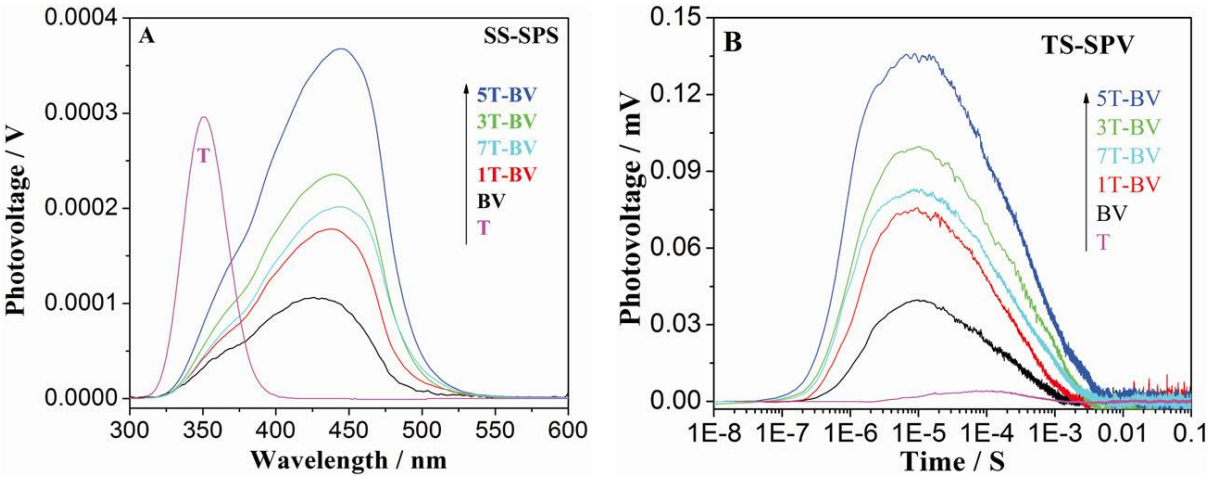

Figure 17: Steady-state and transient-state surface photovoltage spectra for $BiVO_4/TiO_2$ composites. Figure taken from Ref. [62] © 2013 WILEY-VCH Verlag GmbH & Co. KGaA, Weinheim.

Visible driven hydrogen production from water has been observed on $CuS/Zn_{0.8}Cd_{0.2}S$ composites, which have been shown to possess improved charge separation compared to CuS through SS-SPV. The TS-SPV measurement suggested photogenerated electrons transfer from $Zn_{0.8}Cd_{0.2}S$ to CuS.[180] Osterloh and Zhao[181] recently reported the use of SPV spectroscopy to probe carrier dynamics in

nanocrystal films of $HCa_2Nb_3O_{10}$. For sufficiently thick films the SPV spectrum was used to evaluate the efficiency of photochemical charge separation at the sample–support (Au) interface, which revealed that the photovoltage increases linearly with film thickness and that in the presence of an electron blocking PEDOT:PSS layer, the signal arises from electron transfer across the nanocrystal–gold interface. Similarly, $BiVO_4/Co_3O_4$ composites were demonstrated to have significantly improved activity for water oxidation under visible irradiation (11 mmol/h/g);[182] SS-SPV measurement revealed p-type character for the Co_3O_4 particles and a junction at the Co_3O_4–$BiVO_4$ interface, resulting in improved electron–hole separation due to hole injection into Co_3O_4. SPV has also been used to show improved charge separation in other visible driven heterojunction catalysts, such as Ag/Ag_3PO_4/graphene,[183] NiS/CdS,[184] Mn/ZnO[185] and $V_2O_5/BiVO_4$.[186]

5. Theoretical modelling of photocatalyst junction structures

In order to determine the effects of junctions on the charge separation properties of hybrid materials, such as semiconductor heterojunctions A_XB_Y where A_X denotes semiconductor A and B_Y denotes semiconductor B, it is important to establish the relative positions of the valence band and conduction band edges, and so the band offsets of the junction materials, see Figure 18.[16,187] In the absence of electric fields, photogenerated charge carriers will migrate so that photoelectrons will move towards the material with the lowest valence band edge (VBE), and photoholes migrate towards the material with the highest conduction band edge (CBE).[188] The mobility of these charge carriers is modulated by the properties of the band structure, specifically the curvature of the bands in reciprocal space.[189] The conductivity of materials is strongly weighted by the Fermi level position, which represents the electron chemical potential, with *n*-type semiconductors having good photoelectron conductivity and *p*-type semiconductors having good photohole mobility. The Fermi level for a junction will be shifted from the Fermi levels of the two separate materials, as in a real junction the Fermi levels must align

when the two materials are in equilibrium.[190] Furthermore, when two materials with differing Fermi levels are first brought into contact there will be a discontinuity in the Fermi level at the interface. This will cause electron transfer from the material with the higher Fermi level to the lower Fermi level towards an equilibrium. Furthermore the transfer of electrons from one material to another may result in the build-up of a dipole layer at the interface between the two materials, further modifying the relative band positions.[191]

There are thus several physical mechanisms that need to be modelled in order to understand and predict the behaviour of semiconductor heterojunctions for photocatalysis; the relative positions of the band edges of individual materials, which would provide the thermodynamic limits that determine the band offsets; the electronic structure of materials, which would provide information on the charge separation properties of photocatalysts such as electron and hole mobility; and the nature of the junction; which would provide final information on the alignment of bands and the magnitude and effects of any interface dipoles present. In this section we will review the applications of Density Functional Theory (DFT) calculations to treat these problems. Typically these types of calculations can only model systems with a maximum size of a few thousand atoms.[192,193] Based on these size limitations, and as plane wave basis sets typically offer the most efficient calculation of *ab initio* forces, simulations typically focus on crystalline materials representative of bulk systems. Furthermore, DFT is rigorously exact only for ground state properties, such as chemical bonding and cohesive energy. Excited state properties, such as the bandgap and the optical absorption spectra, are not accurately determined. Papers in the literature often report bandgaps as simply the difference in Kohn-Sham eigenvalues between the CBE and the VBE, however DFT tends to underestimate the bandgap, primarily due to the lack of a derivative discontinuity in exchange correlation functionals.[194] Various workarounds have being implemented in order to improve the accuracy of DFT bandgaps. For metal oxide systems two approaches are commonly used, DFT+U where the localisation problem of DFT[195] is treated by the addition of an empirical on-site Coulomb term +U,[196] and hybrid functionals where a proportion of exact Hartree-Fock exchange is added to prompt electron localisation on specific sites.[197,198,199,200] Calculation of excited state properties via the time dependent

Density Functional Theory, or the GW approach, are typically limited to studies of clusters,[201,202,203] and will not be discussed further in this review.

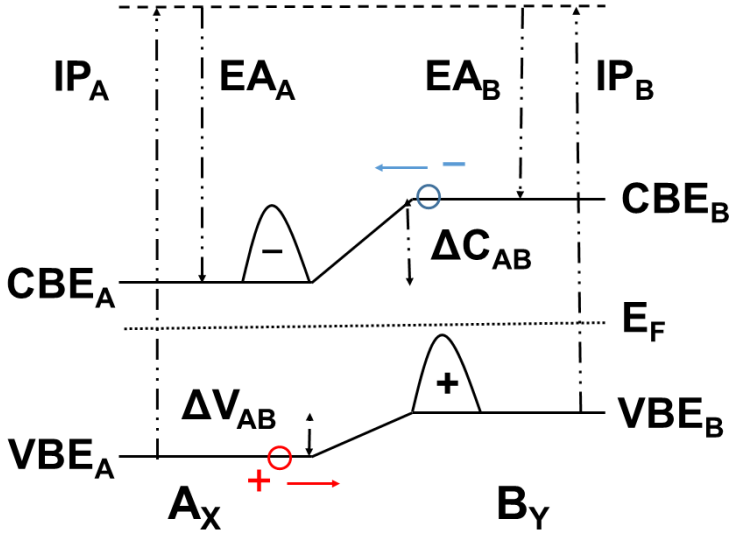

Figure 18: Illustration of the band diagram of a prospective semiconductor Type II heterojunction. After Fermi level alignment, material A_X has a more negative valence band and conduction band energy than material B_Y, as determined by the bulk ionisation potentials (IP) and electron affinities (EA) of both materials, e.g. electronic properties far from the interface. The valence band offset (ΔV_{AB}) and the conduction band offset (ΔC_{AB}) of the material junction can thus be determined. Photoelectrons travel from material B towards material A, whereas photoholes travel from material A towards material B. If the junction has a lot of trapping sites, then charge can accumulate, forming a dipole as illustrated here.

5.1 Computational predictions of material natural band offsets

A good initial guide to determining the flow of charge carriers from one semiconductor to another is the relative position of band edges and the band offsets of the semiconductor heterojunction. To do this requires the establishment of a common reference level for both materials. This is because for bulk periodic systems the energy levels are only defined with respect to an arbitrary constant.[204] The natural choice for a reference is the vacuum level, as found from surface slab calculations with a large vacuum spacing to separate mirror images. The vacuum level may also in principle simply be obtained by a calculation of the ionisation potential of the material, however to implement this in periodic DFT supercell calculations is not trivial. Electronic binding energies are very difficult to obtain, either experimentally or theoretically.[205] Additionally, for periodic DFT supercells there needs

to be an accurate treatment of the long-range electronic polarisation induced by the removal of charge.[187] We note that although there is a large amount of literature on semiconductor band offsets in general, the vast majority focus on materials for electronic applications and solar cells, with little focus on photocatalysis.[206] When we discuss bands being higher or lower than other bands this is all in relation to the vacuum level, for example the VBE of material A_X at –3.5 eV is higher than the VBE of material B_Y at –3.8 eV, therefore photoholes in the valence band will flow from material B_Y to A_X.

In principle, the relative positions of the band edges for semiconductors can be determined by the ionisation potential (IP for the VBE position) and the electron affinity (EA for the CBE position) of the two separate materials. Experimental values of these properties can be used to fix the positions of bands.[207] For materials where only one of these parameters is known, highly accurate hybrid functionals may be used to extrapolate the other property from bandgap calculations, for example the bandgap plus electron affinity is equal to the position of the valence band edge. For many materials however neither the IP nor EA are well characterised, in particular when impurities are present. For these situations we need to calculate the band offsets explicitly. The vacuum energy of the surface slab models is taken to be the electrostatic potential of the supercell at the point where it plateaus, see Figure 19, with the natural VBE and CBE levels determined from explicit comparison of KS eigenvalues with this reference potential. This approach has been used to determine the band positions of several materials, including SnS,[208] Zn_3N_2,[209] In_2O_3,[210] $CuInS_2$,[211] AlN, GaN, InN, and InGaN.[212] As the vacuum reference level requires a surface, two-dimensional materials, such as MoX_2 and WX_2 dichalcogenides (where X = S, Se, and Te),[213] and C_3N_4[16,214] are well suited to this analysis. Martin *et al.* demonstrate, using the vacuum reference approach, that hydrogenation lowers the CBE with respect to the vacuum level, reducing the overpotential for H^+ production and thus reducing the efficacy of the material for hydrogen production.[16] The band alignment of graphitic carbon nitride with the ternary photocatalyst Zn_2GeO_4 has also being recently calculated using the vacuum reference approach.[214] Sun *et al.* determined that this semiconductor heterojunction will be a type II junction, with the C_3N_4 valence and conduction bands higher in energy than the Zn_2GeO_4 valence and conduction bands. Photoelectrons will transfer from C_3N_4 to Zn_2GeO_4 and photoholes will transfer

from Zn_2GeO_4 to C_3N_4. For a correct determination of band offsets for experimental materials the correct surfaces need to be compared as there can be quite a large variability in the work function of surfaces. For example, the calculated work function of $Cu_2O(100)$ is 7.25 eV, whereas for bulk Cu_2O it is 4.84 eV.[215]

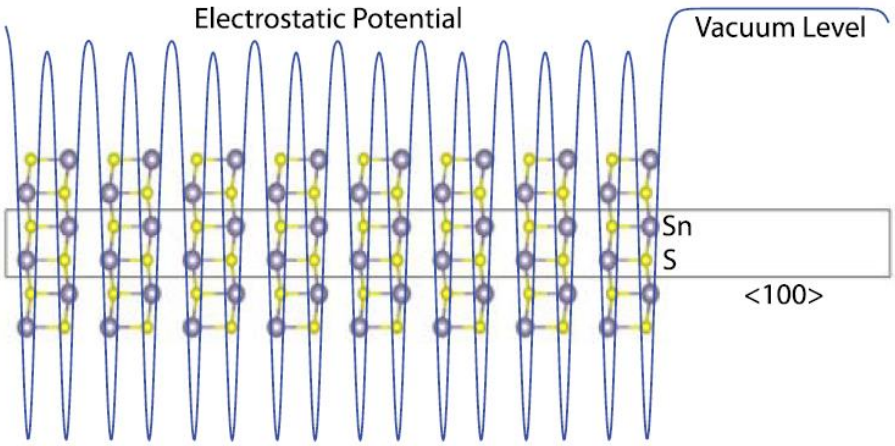

Figure 19: Demonstration of the vacuum reference approach, for SnS. In the bulk of the material the electrostatic potential oscillates rapidly, but in the vacuum the potential plateaus. This plateau provides a value for the energy of the vacuum in this particular simulation, which may then be aligned with the vacuum levels of other periodic calculations. Reprinted with permission from reference [208]. Copyright [2013], AIP Publishing LLC.

There are several papers that report calculations of the ionisation potential of semiconductors using a QM/MM methodology. In this approach, a cluster model of the semiconductor is treated with a quantum mechanical (QM) model, while the cluster is embedded in a molecular mechanical (MM) model.[216,217] This has the advantage of both an accurate description of the electronic degrees of freedom with the QM approach, with an accurate treatment of the long range polarisation effects with the MM approach. This methodology has being used to accurately determine the ionisation potentials and electron affinity of the two main photocatalytic phases of TiO_2, anatase and rutile, with the finding that anatase has the greater electron affinity and ionisation potential and thus has a lower VBE and CBE than rutile. The alignment is Type II, with photoelectrons transferring from rutile to anatase and photoholes transferring from anatase to rutile.[187] This has important implications for charge separation, and the results have been confirmed by other theoretical and experimental work.[218,219]

Similar embedding work has being performed for the solar cell material ZnO.[220] There are relatively limited theoretical efforts on some of the more recent systems under experimental investigation.

5.2 Computational simulation of heterojunctions

So far we have considered band offset determination by calculation of band edges with respect to the vacuum reference level. Implicit in this discussion are several assumptions. Firstly, that an ideal surface without reconstruction or passivation is the best choice for supercell slab simulation. This might not be the case for covalent materials, or indeed for metal oxides with a significant amount of covalency in their electronic structure. Secondly, calculated band offsets may vary for different junctions, e.g. the $A_X([100])/B_Y([101])$ junction should have a different band offset than the $A_X([100])/B_Y([100])$ junction, but without detailed experimental information on the structure of the junction the wrong surfaces may be compared. Thirdly, as outlined above there may be a potential charge transfer from one semiconductor to another when the heterojunction is formed, resulting in the formation of an interface dipole. This will modify the natural band offsets. For all of these reasons, ideally calculations should determine the band offsets of semiconductor heterojunctions directly by the modelling of periodic heterojunctions, for example in Figure 20. Again, as for the calculation of band offsets of separate materials, there are very few theoretical works that focus on metal oxides, therefore in our overview of calculations below we mostly focus on semiconducting materials for electronic applications.

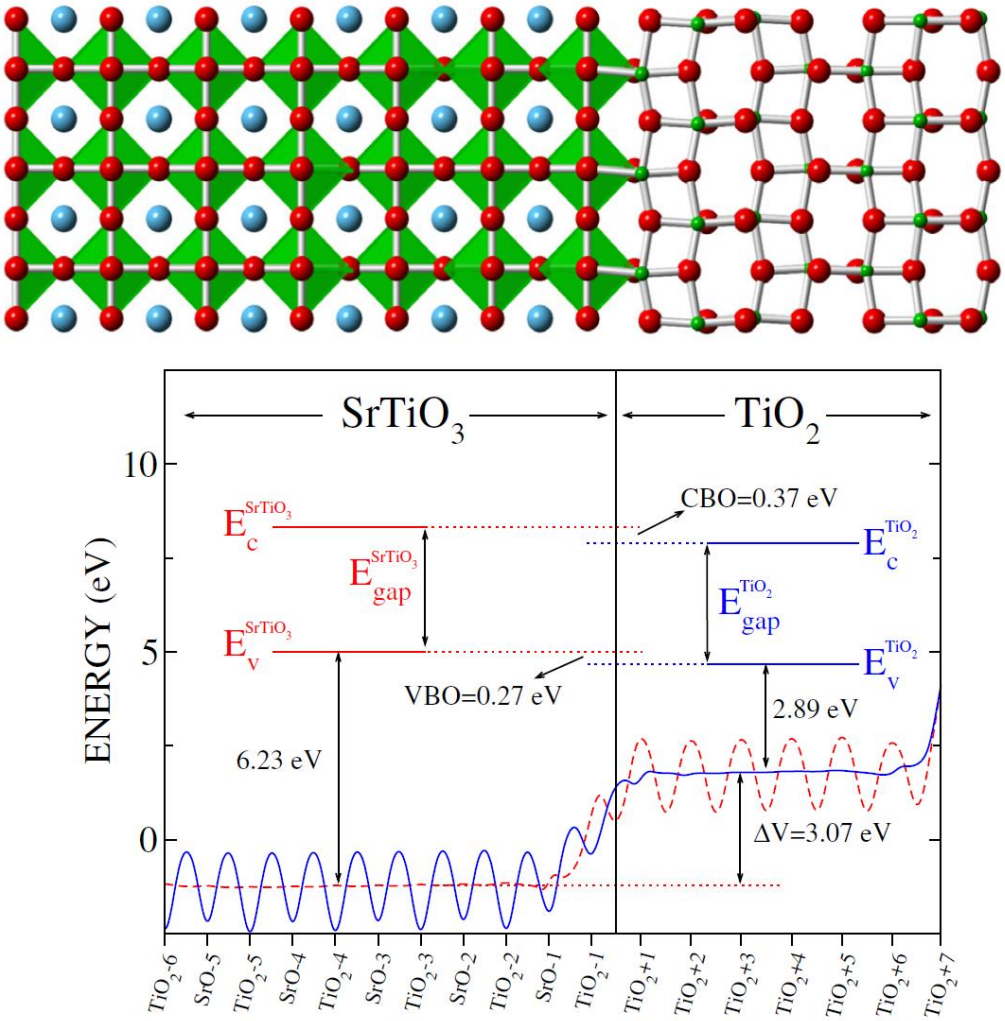

Figure 20: (Top) Example of an *ab initio* simulation of a heterojunction between $SrTiO_3$ (on the left) with anatase TiO_2 (on the right). Sr is represented by blue spheres, Ti by green spheres, and O by red spheres. (Bottom) Schematic of band alignment clearly showing the Type-II interface between the materials. Adapted with permission from reference [221]. Copyright [2012], AIP Publishing LLC.

Before construction of a supercell heterostructure, one fundamental condition needs to be met. Namely, that the terminating surface of each slab is electrically neutral. For example, the rutile TiO_2-(110) surface is neutral, however the Fe_2O_3 (0001) is polar. Therefore an interface between the two materials would involve a substantial amount of reconstruction on the iron oxide surface. Once heterostructures are constructed in the supercell, band offsets cannot be constructed using the vacuum reference approach. Rather, three other methods may be used. The first method is the lineup average electrostatic potential at the interface method of Van de Walle and Martin,[222] the second is the core-

level alignment method of Wei and Zunger,[223] and the third is the local density of states approach of Bass *et al.*.[224] In the first approach, the valence band and conduction band offsets are determined from two terms:

$$VBO = \Delta E_{VBM}^{(B-A)} + \Delta V^{B-A}$$

where $\Delta E_{VBM}^{(B-A)}$ is the bulk band offset and $+\Delta V^{B-A}$ is the interface lineup total potential. The latter quantity can be calculated by taking the macroscopic average of the planar average of the local reference potential $V(z)$, as obtained using

$$\bar{V}(z) = \frac{1}{a}\int V(z - z')\theta(z')dz'$$

where a is the lattice constant and $\theta(z')$ is a unit step function defined as 1 when $-a/2 \leq z' \leq a/2$. This approach has being used to model many materials intefaces, including AlAs/GaAs, AlP/GaP, Si/GaP, Ge/GaAs, Ge/AlAs, Ge/ZnSe, ZnSe/GaAs,[191] ZnO/Cu_2O,[225] InN/GaN,[226] CdTe/CdS, CdS/ZnS, InP/GaP,[211] and AlN/GaN.[227] Using this approach Zemzemi *et al.* looked at the interface between the Cu_2O(111) surface and the ZnO(0001) surface, using the hexagonal CdI_2 polytype structure that is stable under high pressure in order to minimize the lattice mismatch between the two materials.[225] This is to minimize the lattice mistmatch between the two materials. Using the electrostatic potential method they found that their calculated offsets agreed with the experimental value of 1.7 eV. Steiner *et al.* have recently performed a wide-ranging study on lattice matched semiconductor heterojunctions using a variety of methods, include hybrid functionals and the one-shot G_0W_0 approximation.[191] They found that the position of the band edges critically depends on the method used, with accuracy improving with the accuracy of the calculated band-gaps, however, the

interface dipole is well described even with semi-local density functionals. Furthermore, these authors quantified the error in their calculated valence band offsets for the Si/GaP and Ge/AlAs interfaces. Specifically, the large error compared to experiment is associated with the large dipole moment that builds up on the interface due to the charge transfer from one material to the other, see Figure 21.

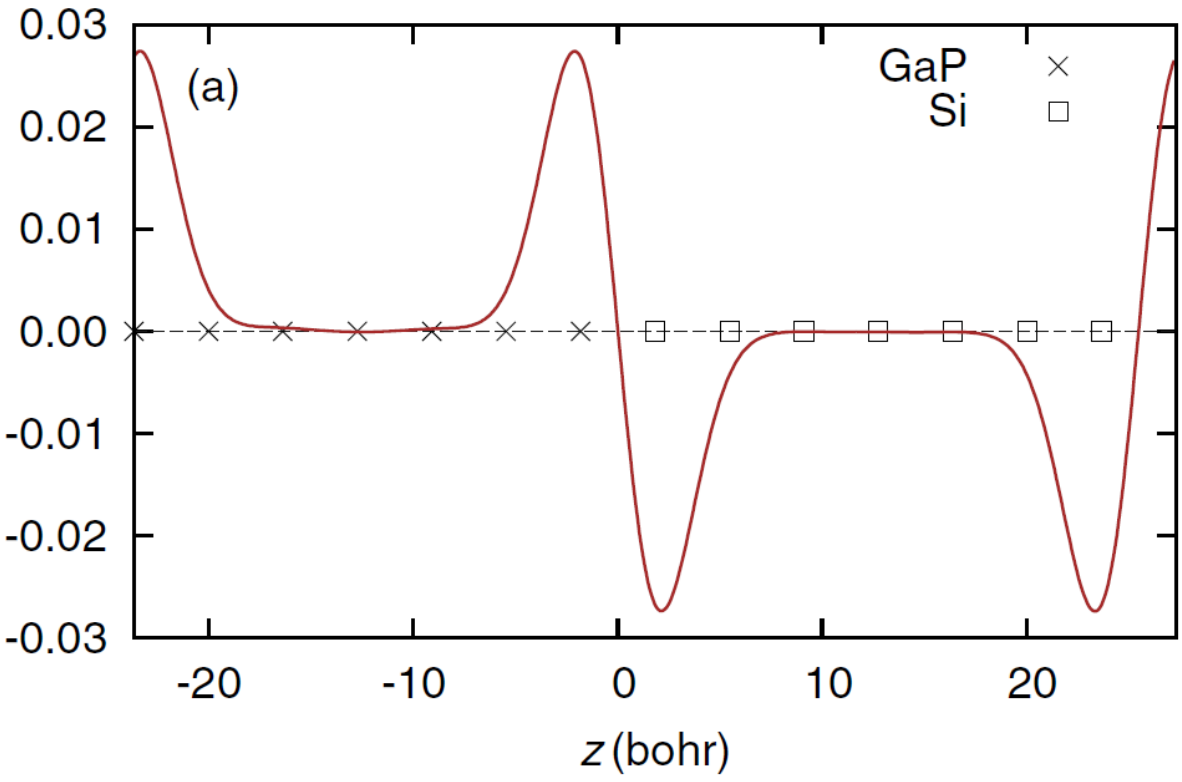

Figure 21: Macroscopic total (electronic and ionic) charge density through the (110) direction of the supercell simulation of the Si/GaP heterojunction. The formation of the dipole along the interface is clearly indicated. Reprinted with permission from Reference [191]. Copyright (2014) by the American Physical Society.

In the second approach, it is assumed that any shift in the core-levels of the atoms is due purely to the change in the neighbouring electrostatic environment, e.g. that the chemical binding does not change the core-levels. To accurately calculate these shifts, three basic steps need to be followed.[228] Firstly, for the isolated materials the energy difference between the core-levels and the valence band maximum may be calculated. This will give a bulk band offset

$$\Delta E_v(A_X/B_Y) = \Delta E_{v,C}(B_Y) - \Delta E_{v,C}(A_X)$$

where $\Delta E_{v,C}(A_X) = E_v(A_X) - E_C(A_X)$ is the energy difference between valence band maximum *v* and the core level *C*. The second step is to determine the shift in core states when an interface is constructed. This involves looking at the core-levels of atoms deep in the interior of each component material in the heterojunction, and calculating the difference, $\Delta E_{C,C'}(A_X/B_Y) = E_{C'}(B_Y) - E_{C'}(A_X)$ where $E_{C'}(B_Y)$ is the energy of the core level of the semiconductor B_Y in the semiconductor heterojunction and $E_{C'}(A_X)$ is the energy of the core level of the semiconductor A_X in the semiconductor heterostructure. This is added to the first term. The final step is to include any effects due to lattice mismatch or compression. Typically heterostructure calculations are performed for an average lattice parameter that is the average of the lattice parameters of the two semiconductors. This means that the bands of both materials will be distorted, and this effect can be determined by investigating the changes in the VBM state for a material by calculating a series of absolute uniaxial deformation potentials for the core state, and mapping onto the valence state (a^{VBM}). This is determined for both A_X and B_Y, and then added to terms one and two, weighted by the relative volume difference $\Delta V/V$. The final expression for the band offset is thus:

$$\Delta E_v(A_X/B_Y) = \Delta E_{v,C}(B_Y) - \Delta E_{v,C}(A_X) + \Delta E_{C,C'}(A_X/B_Y) + a^{VBM}\Delta V/V.$$

This alignment approach has being used successfully to model heterointerfaces, including ZnSe/Zn_3P_2, CdS/Zn_3P_2 and ZnO/Zn_3P_2,[207] CdS/SnS,[229] CdS/Cu_2-ZnS_4,[230] Cu_2/$ZnSnS_4$/ZnO,[231] and TiO_2/$SrTiO_3$.[232] Ichimura calculated the band alignment of the CsS/SnS heterojunction. Using the rocksalt and zincblende structures for SnS they predicted a Type I heterojunction,[229] however

experimentally it is Type II.[233] This reflects the influence of crystal structure on electronic properties, as the actual crystal structure of SnS is orthorhombic. Chambers *et al*. performed calculations and experiments on the epitaxial interface between anatase TiO_2 (001) and $SrTiO_3$ (001). Experimentally there is a valence band offset of 0.16 ± 0.05 eV for thick anatase films, however the calculated theoretical offsets are much larger at 0.54 ± 0.05 eV.[232] Further work by D'Amico *et al.* and Seo *et al.* have demonstrated that oxygen vacancies are responsible for reducing the band offset, as the removal of an oxygen ion induces reconstruction of the surrounding oxygen ions into the TiO_2 surface, decreasing the lattice polarisation and reducing the band offset.[221,234] This work reveals two things: Firstly, these heterojunctions are not likely to charge separate photoelectrons and photoholes; Secondly that the observed band offsets of these interfaces are not intrinsic and may be modified by suitable interface engineering, see Figure 22.

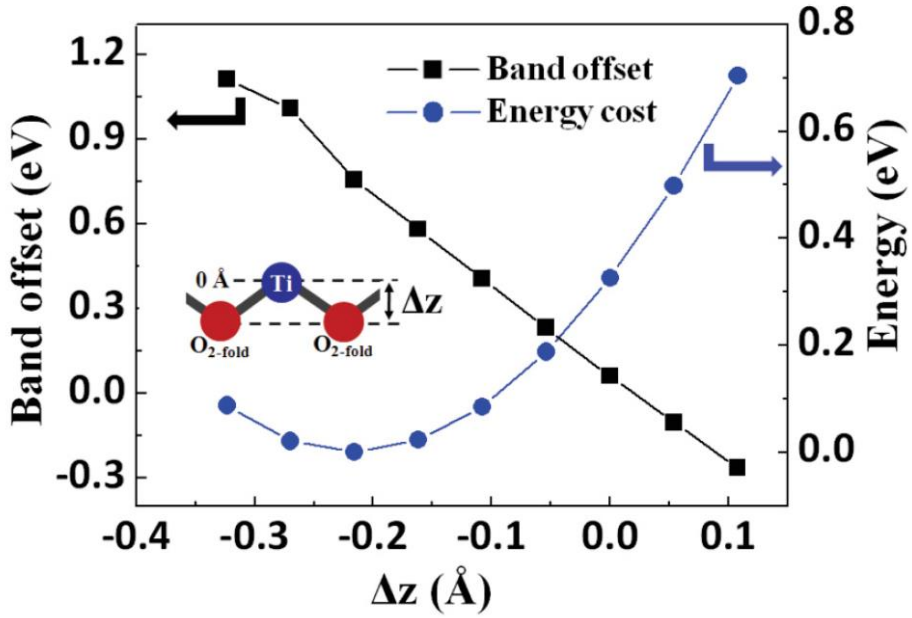

Figure 22: Calculated relationship between the valence band offset of the $SrTiO_3$(001)/anatase TiO_2 (101) interface and the oxygen ion displacement. Figure taken from Reference [234].

In the last method, the local density of states (LDOS) is used to align material bands.[224] Here, highly accurate calculations of the local density of states at the semiconductor heterojunction are performed. The LDOS provides electronic structure information as a function of energy and position. Effectively,

the LDOS can reveal the nature of the heterostructure atoms far from the heterojunction. If the LDOS for these atoms are similar to the LDOS for the bulk semiconductor band edges, then the band edges may be assigned to those atoms. The band offsets between the two semiconductors may thus be determined as a simple energy difference in the local DOS (LDOC). Furthermore, as the LDOS is a function of space, the band bending near the interface may be determined by scanning the LDOS near the interface. The disadvantages of this approach are that all convergence criteria must be stricter, and larger supercells must be used as the LDOS convergence to bulk features is far slower than that of the charge density.[235] This method has being used to calculate the band edges of several interfaces, including BiOCl/Bi_2WO_6,[236] AlAs/GaAs,[237] CdSe/CdTe,[238] AlP/GaP,[239] Si/SiO_2,[240] and Si/WO_3.[241] In the work of Wang *et al.* the authors considered the nature and size of band offsets between the (001) surface of BiOCl and the (010) surface of Bi_2WO_6. Importantly, to align the two surfaces, the lattice parameter of the Bi_2WO_6 surface is extended by 1%, and the BiOCl surface is rotated by 45°. They found that the junction formed was Type I. However, no improvement in charge separation properties as the VBE and CBE of Bi_2WO_6 are straddled by the band edges of BiOCl. However, the doping of sulphur atoms along the interface was found to change the junction to a Type II junction with the VBE and CBE of Bi_2WO_6 lower than that of BiOCl, This would improve charge separation properties, as photoelectrons would flow from BiOCl to Bi_2WO_6 while photoholes would flow from Bi_2WO_6 to BiOCl.[236] Wang *et al.* also looked at the band offsets of the Si(001)/WO_3(100) interface. They found that this junction would result in a Type II interface, see Figure 23, with the silicon VBE and CBE higher than that of WO_3. Photoholes would travel from WO_3 to Si in this material, however as the CBE of silicon is higher than the CBE of WO_3 in their simulations, the small Schottky barrier of 0.5 eV would prevent electron transfer from WO_3 to Si. For this junction to have the greatest charge separation efficiency, care must be taken to modify the interface layer.[241]

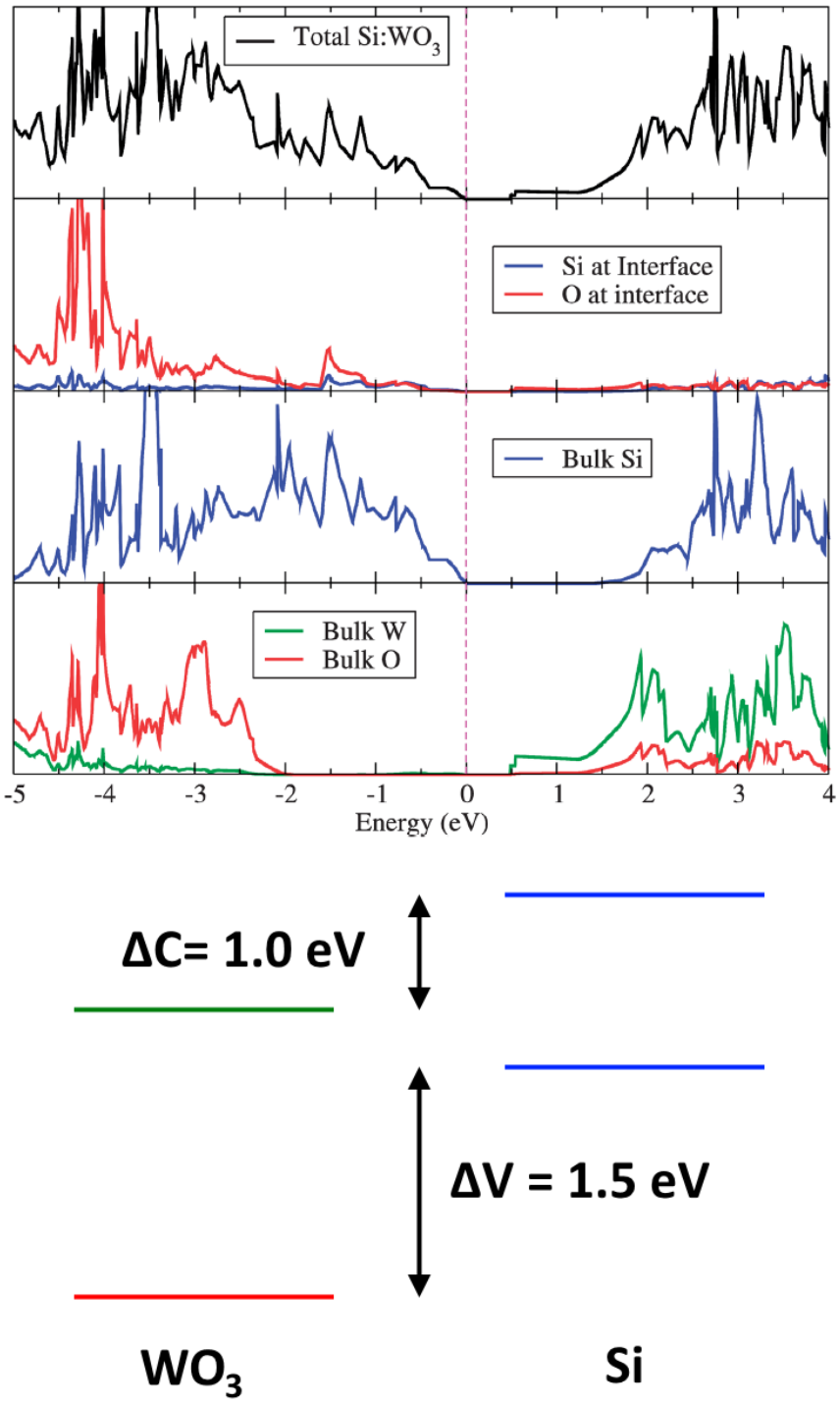

Figure 23: Electronic density of Si(001)/WO_3(100) interface (top) and calculated band alignment (bottom). The Type II alignment can be clearly seen, with the empty states associated with WO_3 below the empty states associated with Si, and the full states associated with Si above the full states associated with WO_3. Adapted from Ref. [241] with permission from The Royal Society of Chemistry.

One important point it is essential to emphasize when discussing the simulation of explicit heterojunctions is the tendency of density functionals to underestimate the bandgap. A common method to correct the bandgap is the hybrid density functional theory, wherein a percentage of exact exchange is mixed into the functional. The greater the percentage of the exact exchange, the larger the gap. However, a major issue with hybrid functionals is that they are computationally much more expensive, therefore geometry optimisation is typically undertaken using a GGA functional, with analysis of the final structure made using a hybrid functional. Furthermore, the amount of exact exchange (α) is material dependent, with the percentage of exact exchange typically $\alpha = 1/\varepsilon_\infty$, where ε_∞ is the electronic dielectric constant of the material.[242] In DFT simulations a single hybrid functional must be used, therefore for two materials with different bandgaps a choice of α must be made, at least one of the bandgaps will be in error. This problem can be managed by using the electrostatic potential in the solid as the common reference potential. Work performed by Ramprasad *et al.* demonstrates that the position obtained for a defect level in a semiconductor m if referenced to the electrostatic potential, is independent of the functional used.[243] Therefore, the procedure is as follows, for each pure phase gap edges are determined with respect to the electrostatic potential, then the potential in an interface model is computed with some functional, and both results are combined to determine the relative band edge positions. This approach was used by Conesa, who used hybrid DFT to determine the band alignment at the ZnO-(110)/anatase TiO_2-(001) surface.[244] Using α values of 0.16 for TiO_2, 0.267 for ZnO, and 0.22 for the heterojunction simulation, he found that ZnO has lower energy conduction and valence bands than TiO_2, thus forming a Type II junction and demonstrating why ZnO decorated with TiO_2 has superior solar cell characteristics than isolated ZnO.

So far we have considered bulk heterojunction interfaces. This often necessitates the averaging of lattice parameters, however it is open question whether in real systems this would occur. For example,

often in experimental systems one metal oxide is often decorated with small nanoparticles of another metal oxide, for example, TiO_2 nanosheets decorated with 2nm FeO_x, CoO_x, NiO_x, and CuO_x clusters.[97,245,246] An alternative model for simulating these kinds of junctions would involve the interaction between a metal oxide surface, represented using a slab model, and a metal oxide nanoparticle. DFT calculations generally consider the interaction of small (one or two formula unit) metal oxide clusters on rutile (110) and anatase (110) surfaces. Furthermore, these calculations explicitly mix two different materials together, so more advanced DFT methods that more accurately determine bandgaps should be used, such as the GGA+U approach. Nolan modelled the decoration of rutile (110) with a single Fe_2O_3 unit. This was found to result in a Type II junction with the rutile VBE 0.3 eV below the Fe_2O_3 HOMO state, and the rutile CBE 0.1 eV below the Fe_2O_3 LUMO state.[246] This would favour photohole transfer into the Fe_2O_3 cluster. Further, calculation of the triplet state indicates electron relaxation onto the Fe_2O_3 cluster, see Figure 24. Moniz *et al.* modelled the adsorption of Fe_2O_3 and Fe_2O_3 clusters on anatase (101). They found a more complicated picture. The interface between metal oxides is Type III, with the HOMO and LUMO of the Fe_2O_3 clusters straddled by the band edges of the anatase slab. For the Fe_2O_3 cluster the VBE of anatase is 0.4 eV lower in energy than the HOMO state of the cluster, whereas for the $(Fe_2O_3)_2$ cluster it is 1.0 eV lower in energy than the HOMO state of the cluster. In contrast, the CBE of anatase is 0.65 eV higher in energy than the LUMO of the Fe_2O_3 cluster, and 0.6 eV higher than the LUMO of the $(Fe_2O_3)_2$ cluster.[97] For the smaller cluster the greater thermodynamic driving force towards charge separation is for the photoelectrons, whereas for the larger cluster it is for the photoholes. Experimentally, results indicate photoelectron separation into the Fe_2O_3 cluster, implying that kinetic effects further hinder hole transport from anatase to Fe_2O_3.

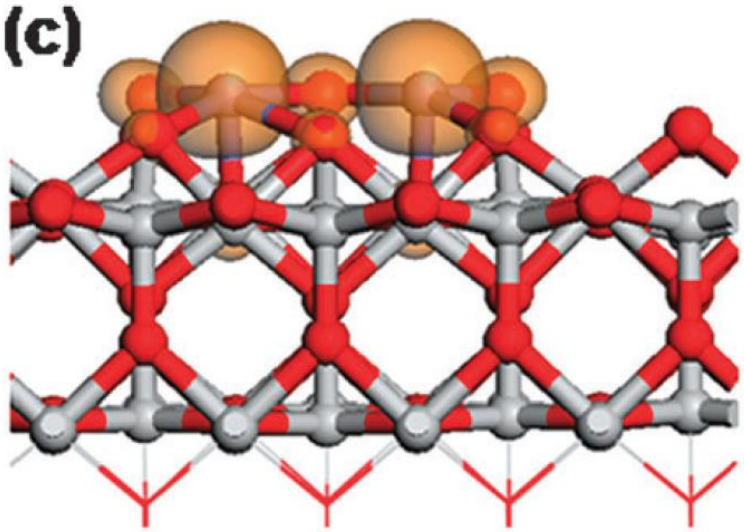

Figure 24: Spin density of the triplet state for the Fe_2O_3 modified rutile surface. Both photoelectron and photohole reside on the Fe_2O_3 cluster. Adapted and reproduced from Ref. [241] with permission from The Royal Society of Chemistry.

For a complete understanding of heterointerfaces the modeller must also factor into account the stability of the junction. For the metal oxide clusters discussed above the binding energies are rather large, with exothermic binding on the order of 4.00 eV per cluster. Those clusters are very small though, and would be expected to be reactive. Sun *et al*. have modelled the interaction of multiple layers of graphitic carbon nitride (001) surface with the Zn_2GeO_4 (110) interface. The adsorption energy was exothermic, with an adsorption energy of 0.18 eV/Å^2, with additional g-C_3N_4 sheets not modifying the interfacial binding properties.[214] Bendavid *et al*. have investigated the adhesion of the Cu_2O-(111) surface to the ZnO–$(10\bar{1}0)$ surface.[247] They found that the interface was stable, with a weakly exothermic adsorption energy of 0.05 eV/Å^2. The Cu_2O is modelled as an overlayer on the ZnO surface, the most stable overcoating of Cu_2O was found to be three overlayers. The strain field along the interface must also be considered. For many of the semiconductors heterointerfaces studied the materials are isovalent and isostructural. This is not the case for many potential metal oxide junctions though, where different structures may be joined together, with different ionic charges and binding motifs, and with different lattice parameters. Lattice mismatch must be accommodated, either by clever construction of interface models as by Wang *et al.* [236] or by some sort of averaging of lattice

parameters, *e.g.* by strain energy or simple geometry. We would expect that strained lattices are prone to misfit dislocation or defect generation, in order to relieve strain. These defects could then modify band offsets, as demonstrated D'Amico *et al.* and Seo *et al.*[221,234] Recent theoretical work by Hinuma *et al.* on the interfaces of CdTe/CdS, CdS/ZnS, and InP/GaP have investigated, using a GGA functional, the effects of misfit dislocations on the band offsets.[211] For these materials, dislocations approximately 1 nm from the interface modify the valence band offset by ~ 0.1 eV.

Conclusions and outlook.

The development of a low-cost strategy to increase the solar-to-hydrogen conversion efficiency is a fundamental part of our search to find renewable and sustainable energy sources. In order to attain the US Department of Energy's device efficiency target of over 10%, a new materials strategy is required to develop stable, efficient photocatalyst materials that can operate under solar irradiation. One of the fundamental problems to address in semiconductor photocatalysts is the dynamics of the charge carriers which do the useful work, in a realm where more often than not, very fast recombination is the dominating factor. We have also put forward some viable strategies to increase efficiency. One must carefully select materials with good visible light absorption and appropriate band positions and alignment so that charge transfer may be thermodynamically feasible. It goes without saying that nanostructuring is a key attribute of any catalyst material, however careful tuning of the morphology, either through facet engineering, texturing/1D alignment (for light trapping), increase in bulk porosity or minor surface modification are just a few steps that can dramatically enhance the activity of a good water splitting photocatalyst. Indeed the particle transfer method for development of compact photoelectrodes recently proposed by Domen[248] has great promise in this area, because it facilitates improved charge transfer between particles to counter electrode and permits the use of pre-formed particles (which are highly active in suspension-based photocatalysis systems) to be utilised as photoelectrodes. The role of plasmonic layers and ultra-high energy electrons represent just a few of the very recent breakthroughs concerning our fundamental understanding of charge transfer and more

work is needed to fully realise their potential. The relatively recent progress in the utilisation of strategies to efficiently separate charges through Z-scheme photocatalysts, homojunctions and surface passivation layers require further investigation to understand the charge transfer mechanism. We too, believe the four key types of junction that show the greatest potential in terms of efficiency are as follows: (a) the coupling of semiconductors with other semiconductors to satisfy high absorption of solar energy and to create sufficient built-in potential for redox reactions; (b) the formation of heterostructured junctions with conductive carbon-based materials to effectively drive the separation and transportation of the electron–hole pairs; (c) the deposition of metal species to enhance the utilization of sunlight or improve the separation and transportation of the electron–hole pairs; (d) the forming of multicomponent heterojunctions for enhancing the utilization of sunlight and improving the separation/transportation of charge carriers.[30] From these preliminary studies, we think junctions involving carbon-based materials will lead to a robust, low-cost system for water splitting if an efficient junction can be fabricated using a stable sensitizer.

Overall, we have demonstrated that the concept of a heterojunction architecture is an emerging and clearly viable route to increasing efficiency and improving stability by facilitating improved charge separation and transfer; the evidence of which is discussed herein with our review of a wealth of very recent reports on the photocatalytic properties of visible-light driven heterojunction photocatalysts. By far the most common methods to investigate charge separation and transport on such timescales involve the use of advanced spectroscopy techniques and these may enable us to address the underlying reasons for low efficiencies in water splitting reactions. It is clear that TAS, in particular, is becoming an established method to investigate charge carrier dynamics in semiconductors and solar cell devices.

Computer simulation of heterointerfaces is an ongoing and exploratory field of scientific research. From our overview we can conclude that we are well-placed to determine the band offsets of bulk materials, however the simulation and understanding of the electronic structure of metal oxide interfaces is still somewhat tentative. Great care must be taken to accurately model the interface dipole, strain field effects, and defects. Care must also be taken to accurately model the physical

structure of the interface, as the crystal structure can have a significant effect on the band offsets. The methodologies and computer resources are present for at least a qualitative understanding and prediction of these effects, and to enable further optimisation of these hybrid systems.

Thus we have demonstrated that semiconductor heterojunctions are a viable approach for efficient hydrogen fuel generation and that significant advances have been achieved in their design and construction over the last ten years. Although their solar-to-fuel conversion efficiencies are still some way off from meeting the criteria for commercialization, we hope that through developing a fundamental understanding of charge transfer in these systems (either through theoretical modelling or spectroscopic techniques), this will facilitate the fabrication of more efficient junction architectures. Research on this topic is large and is expanding rapidly. Our review discusses the state-of-the-art, and indicates experimental and theoretical approaches that can be used to further improve understanding and performance of these complicated and interesting systems.

Acknowledgements

All authors acknowledge financial support from EU FP7 (4G-PHOTOCAT 309636) and J. Tang thanks The Leverhulme Trust for financial support (RPG-2012-582).

References

1. A. Kudo and Y. Miseki, *Chemical Society Reviews*, 2009, **38**, 253–278.
2. K. Li, D. Martin, and J. Tang, *Chinese Journal of Catalysis*, 2011, **32**, 879–890.
3. R. Marschall, *Advanced Functional Materials*, 2014, **24**, 2421–2440.
4. A. Fujishima and K. Honda, *Nature*, 1972, **238**, 37–38.
5. Z. Li, W. Luo, M. Zhang, J. Feng, and Z. Zou, *Energy & Environmental Science*, 2013, **6**, 347.
6. S. J. A. Moniz, R. Quesada-Cabrera, C. S. Blackman, J. Tang, P. Southern, P. M. Weaver, and C. J. Carmalt, *Journal of Materials Chemistry A*, 2014, **2**, 2922–2927.
7. A. Bard and M. Fox, *Accounts of Chemical Research*, 1995, **28**, 141–145.
8. J. Tang, J. R. Durrant, and D. R. Klug, *Journal of the American Chemical Society*, 2008, **130**, 13885–13891.
9. K. Sivula, R. Zboril, F. Le Formal, R. Robert, A. Weidenkaff, J. Tucek, J. Frydrych, and M. Grätzel, *Journal of the American Chemical Society*, 2010, **132**, 7436–7444.
10. G. Hodes, D. Cahen, and J. Manassen, *Nature*, 1976, **260**, 312–313.
11. C. A. Bignozzi, S. Caramori, V. Cristino, R. Argazzi, L. Meda, and A. Tacca, *Chemical Society Reviews*, 2013, **42**, 2228–2246.
12. K. Sayama, A. Nomura, Z. Zou, R. Abe, Y. Abe, and H. Arakawa, *Chemical Communications*, 2003, 2908–2909.
13. R. Li, F. Zhang, D. Wang, J. Yang, M. Li, J. Zhu, X. Zhou, H. Han, and C. Li, *Nature Communications*, 2013, **4**, 1–7.
14. A. Kudo, K. Ueda, H. Kato, and I. Mikami, *Catalysis Letters*, 1998, **53**, 229–230.
15. D. J. Martin, N. Umezawa, X. Chen, J. Ye, and J. Tang, *Energy & Environmental Science*, 2013, **6**, 3380–3386.
16. D. J. Martin, K. Qiu, S. A. Shevlin, A. D. Handoko, X. Chen, Z. Guo, and J. Tang, *Angewandte Chemie International Edition*, 2014, **53**, 9240–9245.
17. K. Rhee, E. Morris, J. Barber, and W. Kühlbrandt, *Nature*, 1998, **396**, 283–286.
18. D. J. Martin, P. J. T. Reardon, S. J. A. Moniz, and J. Tang, *Journal of the American Chemical Society*, 2014, **136**, 12568–12571.
19. K. Maeda, T. Takata, M. Hara, N. Saito, Y. Inoue, H. Kobayashi, and K. Domen, *Journal of the American Chemical Society*, 2005, **127**, 8286–8287.
20. O. Khaselev and J. A. Turner, *Science*, 1998, **280**, 425–427.
21. K. Sivula, *The Journal of Physical Chemistry Letters*, 2013, **4**, 1624–1633.

22. M. G. Walter, E. L. Warren, J. R. McKone, S. W. Boettcher, Q. Mi, E. a Santori, and N. S. Lewis, *Chemical reviews*, 2010, **110**, 6446–6473.

23. Z. Zhang and J. T. Yates, *Chemical reviews*, 2012, **112**, 5520–51.

24. H. Wang, L. Zhang, Z. Chen, J. Hu, S. Li, Z. Wang, J. Liu, and X. Wang, *Chemical Society reviews*, 2014, **43**, 5234–5244.

25. Q. Xiang, J. Yu, and M. Jaroniec, *Chemical Society reviews*, 2012, **41**, 782–796.

26. X. Huang, X. Qi, F. Boey, and H. Zhang, *Chemical Society reviews*, 2012, **41**, 666–86.

27. H. Tada, T. Mitsui, T. Kiyonaga, T. Akita, and K. Tanaka, *Nature materials*, 2006, **5**, 782–786.

28. T. Hisatomi, J. Kubota, and K. Domen, *Chemical Society reviews*, 2014, DOI: 10.1039/C3CS60378D.

29. A. J. Cowan and J. R. Durrant, *Chemical Society reviews*, 2013, **42**, 2281–2293.

30. H. Wang, L. Zhang, Z. Chen, J. Hu, S. Li, Z. Wang, J. Liu, and X. Wang, *Chemical Society Reviews*, 2014, **43**, 5234–5244.

31. K. Iwashina and A. Kudo, *Journal of the American Chemical Society*, 2011, **133**, 13272–13275.

32. H. G. Kim, D. W. Hwang, and J. S. Lee, *Journal of the American Chemical Society*, 2004, **126**, 8912–8913.

33. X. Xu, C. Randorn, P. Efstathiou, and J. T. S. Irvine, *Nature Materials*, 2012, **11**, 1–4.

34. K. Maeda, M. Higashi, B. Siritanaratkul, R. Abe, and K. Domen, *Journal of the American Chemical Society*, 2011, **133**, 12334–12337.

35. A. Kasahara and K. Nukumizu, *The Journal of Physical Chemistry A*, 2002, **106**, 6750–6753.

36. M. Higashi, K. Domen, and R. Abe, *Journal of the American Chemical Society*, 2012, **134**, 6968–69671.

37. E. Kim, N. Nishimura, G. Magesh, J. Y. Kim, J.-W. Jang, H. Jun, J. Kubota, K. Domen, and J. S. Lee, *Journal of the American Chemical Society*, 2013, **135**, 5375–5383.

38. H. Kim, D. Monllor-Satoca, W. Kim, and W. Choi, *Energy Environ. Sci.*, 2014, DOI: 10.1039/c4ee02169j.

39. J. Hou, C. Yang, H. Cheng, S. Jiao, O. Takeda, and H. Zhu, *Energy Environ. Sci.*, 2014, **7**, 3758–3768.

40. A. Kudo and Y. Miseki, *Chemical Society Reviews*, 2009, **38**, 253–278.

41. A. Kudo, *Catalysis Surveys from Asia*, 2003, **7**, 31–38.

42. A. Walsh, Y. Yan, and M. Huda, *Chemistry of Materials*, 2009, 547–551.

43. F. F. Abdi, L. Han, A. H. M. Smets, M. Zeman, B. Dam, and R. van de Krol, *Nature communications*, 2013, **4:2195**, 1–7.

44. Y. Park, K. J. McDonald, and K. S. Choi, *Chemical Society Reviews*, 2013, **42**, 2321–2337.

45. J. Su, L. Guo, N. Bao, and C. a Grimes, *Nano letters*, 2011, **11**, 1928–1933.

46. S. J. Hong, S. Lee, J. S. Jang, and J. S. Lee, *Energy & Environmental Science*, 2011, **4**, 1781.

47. R. Saito, Y. Miseki, and K. Sayama, *Chemical Communications*, 2012, **48**, 3833–3835.

48. Y. Pihosh, I. Turkevych, K. Mawatari, T. Asai, T. Hisatomi, J. Uemura, M. Tosa, K. Shimamura, J. Kubota, K. Domen, and T. Kitamori, *Small*, 2014, 1–8.

49. X. Shi, I. Y. Choi, K. Zhang, J. Kwon, D. Y. Kim, J. K. Lee, S. H. Oh, J. K. Kim, and J. H. Park, *Nature communications*, 2014, **5**, 4775.

50. S. J. A. Moniz, J. Zhu, and J. Tang, *Advanced Energy Materials*, 2014, **4**, 201301590.

51. L. Zhang, E. Reisner, and J. J. Baumberg, *Energy & Environmental Science*, 2014, **7**, 1402–1408.

52. S. K. Pilli, T. E. Furtak, L. D. Brown, T. G. Deutsch, J. A. Turner, and A. M. Herring, *Energy & Environmental Science*, 2011, **4**, 5028–5034.

53. H. W. Jeong, T. H. Jeon, J. S. Jang, W. Choi, and H. Park, *The Journal of Physical Chemistry C*, 2013, **117**, 9104–9112.

54. F. Abdi and R. van de Krol, *The Journal of Physical Chemistry C*, 2012, **116**, 9398–9404.

55. J. A. Seabold and K.-S. Choi, *Journal of the American Chemical Society*, 2012, **134**, 2186–2192.

56. T. W. Kim and K.-S. Choi, *Science*, 2014, **343**, 990–994.

57. S. K. Choi, W. Choi, and H. Park, *Physical Chemistry Chemical Physics*, 2013, **15**, 6499–6507.

58. P. Chatchai, S. Kishioka, Y. Murakami, A. Y. Nosaka, and Y. Nosaka, *Electrochimica Acta*, 2010, **55**, 592–596.

59. S. K. Pilli, T. G. Deutsch, T. E. Furtak, L. D. Brown, J. a Turner, and A. M. Herring, *Physical chemistry chemical physics*, 2013, **15**, 3273–3278.

60. M. Ma, J. Kim, K. Zhang, and X. Shi, *Chemistry of Materials*, 2014, **26**, 5592–5597.

61. X. Fu, M. Xie, P. Luan, and L. Jing, *ACS applied materials & interfaces*, 2014, **6**, 18550–18557.

62. M. Xie, X. Fu, L. Jing, P. Luan, Y. Feng, and H. Fu, *Advanced Energy Materials*, 2013, **4**, DOI: 10.1002/aenm.201300995.

63. S. Ho-Kimura, S. J. A. Moniz, A. D. Handoko, and J. Tang, *Journal of Materials Chemistry A*, 2014, **2**, 3948–3953.

64. Y. H. Ng, A. Iwase, A. Kudo, and R. Amal, *The Journal of Physical Chemistry Letters*, 2010, **1**, 2607–2612.

65. X. Deng and H. Tüysüz, *ACS Catalysis*, 2014, **4**, 3701–3714.

66. L. G. Bloor, P. I. Molina, M. D. Symes, and L. Cronin, *Journal of the American Chemical Society*, 2014, **136**, 3304–3311.

67. J. Gerken, J. McAlpin, J. Y. C. Chen, M. L. Rigsby, W. H. Casey, J. B. Gerken, J. G. McAlpin, R. D. Britt, and S. S. Stahl, *Journal of the American Chemical Society*, 2011, **133**, 14431–14442.

68. D. K. Bediako, B. Lassalle-Kaiser, Y. Surendranath, J. Yano, V. K. Yachandra, and D. G. Nocera, *Journal of the American Chemical Society*, 2012, **134**, 6801–6809.

69. M. W. Kanan and D. G. Nocera, *Science*, 2008, **321**, 1072–1075.

70. M. W. Kanan, Y. Surendranath, and D. G. Nocera, *Chemical Society Reviews*, 2009, **38**, 109–114.

71. L. Jing, J. Zhou, J. R. Durrant, J. Tang, D. Liu, and H. Fu, *Energy & Environmental Science*, 2012, **5**, 6552–6558.

72. Y. Cao, L. Jing, X. Shi, Y. Luan, J. R. Durrant, J. Tang, and H. Fu, *Physical chemistry chemical physics*, 2012, **14**, 8530–8536.

73. F. F. Abdi, T. J. Savenije, M. M. May, B. Dam, and R. Van De Krol, *The Journal of Physical Chemistry Letters*, 2013, **4**, 2752–2757.

74. T. H. Jeon, W. Choi, and H. Park, *Physical chemistry chemical physics*, 2011, **13**, 21392–21401.

75. D. K. Zhong, S. Choi, and D. R. Gamelin, *Journal of the American Chemical Society*, 2011, **133**, 18370–18377.

76. S. K. Pilli, T. G. Deutsch, T. E. Furtak, J. a Turner, L. D. Brown, and A. M. Herring, *Physical chemistry chemical physics*, 2012, 7032–7039.

77. C. Jiang, S. J. A. Moniz, M. Khraisheh, and J. Tang, *Chemistry - A European Journal*, 2014, **20**, 12954–12961.

78. D. K. Zhong, J. Sun, H. Inumaru, and D. R. Gamelin, *Journal of the American Chemical Society*, 2009, **131**, 6086–7.

79. D. K. Zhong and D. R. Gamelin, *Journal of the American Chemical Society*, 2010, **132**, 4202–7.

80. D. K. Zhong, M. Cornuz, K. Sivula, M. Grätzel, and D. R. Gamelin, *Energy & Environmental Science*, 2011, **4**, 1759–1764.

81. M. Barroso, A. J. Cowan, S. R. Pendlebury, M. Grätzel, D. R. Klug, and J. R. Durrant, *Journal of the American Chemical Society*, 2011, **133**, 14868–14871.

82. M. Barroso, C. Mesa, S. R. Pendlebury, A. J. Cowan, T. Hisatomi, K. Sivula, M. Grätzel, D. R. Klug, and J. R. Durrant, *Proceedings of the National Academy of Sciences*, 2012, **109**, 15640–15645.

83. Y.-R. Hong, Z. Liu, S. F. B. Al-Bukhari, C. J. Lee Jun, D. L. Yung, D. Chi, and T. S. A. Hor, *Chemical Communications*, 2011, **47**, 10653–10655.

84. J. A. Seabold and K. S. Choi, *Chemistry of Materials*, 2011, **23**, 1105–1112.

85. R. Liu, Y. Lin, L.-Y. Chou, S. W. Sheehan, W. He, F. Zhang, H. J. M. Hou, and D. Wang, *Angewandte Chemie International Edition*, 2011, **50**, 499–502.

86. K. Sivula, F. Le Formal, and M. Grätzel, *ChemSusChem*, 2011, **4**, 432–439.

87. S. R. Pendlebury, A. J. Cowan, M. Barroso, K. Sivula, J. Ye, M. Grätzel, D. R. Klug, J. Tang, and J. R. Durrant, *Energy & Environmental Science*, 2012, **5**, 6304.

88. M. Barroso, S. R. Pendlebury, A. J. Cowan, and J. R. Durrant, *Chemical Science*, 2013, **4**, 2724–2734.

89. K. Sivula, F. Le Formal, and M. Grätzel, *Chemistry of Materials*, 2009, **21**, 2862–2867.

90. Y. Hou, F. Zuo, A. Dagg, and P. Feng, *Nano letters*, 2012, **12**, 6464–6473.

91. Y. Hou, F. Zuo, A. Dagg, and P. Feng, *Angewandte Chemie International Edition*, 2013, **52**, 1248–1252.

92. S. D. Tilley, M. Cornuz, K. Sivula, and M. Grätzel, *Angewandte Chemie International Edition*, 2010, **49**, 6405–8.

93. D. K. Bora, A. Braun, R. Erni, U. Müller, M. Döbeli, and E. C. Constable, *Physical chemistry chemical physics*, 2013, **15**, 12648–59.

94. J. Li, F. Meng, S. Suri, W. Ding, F. Huang, and N. Wu, *Chemical communications*, 2012, **48**, 8213–5.

95. H. S. Han, S. Shin, J. H. Noh, I. S. Cho, and K. S. Hong, *JOM*, 2014, **66**, 664–669.

96. K. McDonald and K. Choi, *Chemistry of Materials*, 2011, 4863–4869.

97. S. J. A. Moniz, S. A. Shevlin, X. An, Z.-X. Guo, and J. Tang, *Chemistry - A European Journal*, 2014, **20**, 15571–15579.

98. S. Rai, A. Ikram, S. Sahai, S. Dass, R. Shrivastav, and V. R. Satsangi, *RSC Advances*, 2014, **4**, 17671.

99. M. T. Mayer, Y. Lin, G. Yuan, and D. Wang, *Accounts of chemical research*, 2013, **46**, 1558–1566.

100. Y. Lin, S. Zhou, S. W. Sheehan, and D. Wang, *Journal of the American Chemical Society*, 2011, **133**, 2398–401.

101. Y. Lin, G. Yuan, S. Sheehan, S. Zhou, and D. Wang, *Energy & Environmental Science*, 2011, **4**, 4862.

102. Y. Lin, Y. Xu, M. T. Mayer, Z. I. Simpson, G. McMahon, S. Zhou, and D. Wang, *Journal of the American Chemical Society*, 2012, **134**, 5508–11.

103. M. T. Mayer, C. Du, and D. Wang, *Journal of the American Chemical Society*, 2012, **134**, 12406–9.

104. Z. Yi, J. Ye, N. Kikugawa, T. Kako, S. Ouyang, H. Stuart-Williams, H. Yang, J. Cao, W. Luo, Z. Li, Y. Liu, and R. L. Withers, *Nature materials*, 2010, **9**, 559–564.

105. Y. Bi, S. Ouyang, J. Cao, and J. Ye, *Physical chemistry chemical physics*, 2011, **13**, 10071–5.

106. C. Li, P. Zhang, R. Lv, J. Lu, T. Wang, S. Wang, H. Wang, and J. Gong, *Small*, 2013, **9**, 3951–6, 3950.

107. J. Guo, S. Ouyang, P. Li, Y. Zhang, T. Kako, and J. Ye, *Applied Catalysis B: Environmental*, 2013, **134-135**, 286–292.

108. Y. Hou, F. Zuo, Q. Ma, and C. Wang, *The Journal of Physical Chemistry C*, 2012, **116**, 20132–20139.

109. W. Zhai, G. Li, P. Yu, L. Yang, and L. Mao, *The Journal of Physical Chemistry C*, 2013, **117**, 15183–15191.

110. Y.-G. Lin, Y.-K. Hsu, Y.-C. Chen, S.-B. Wang, J. T. Miller, L.-C. Chen, and K.-H. Chen, *Energy & Environmental Science*, 2012, **5**, 8917.

111. X. Liu, F. Wang, and Q. Wang, *Physical chemistry chemical physics*, 2012, **14**, 7894–911.

112. W. Kim, T. Tachikawa, D. Monllor-Satoca, H. Kim, T. Majima, and W. Choi, *Energy & Environmental Science*, 2013, **6**, 3732–3739.

113. J. Lin, P. Hu, Y. Zhang, M. Fan, Z. He, C. K. Ngaw, J. S. C. Loo, D. Liao, and T. T. Y. Tan, *RSC Advances*, 2013, **3**, 9330.

114. S. S. K. Ma, K. Maeda, R. Abe, and K. Domen, *Energy & Environmental Science*, 2012, **5**, 8390.

115. M. Matsumura and S. Furukawa, *The Journal of Physical Chemistry*, 1985, 1983–1985.

116. H. Yan, J. Yang, G. Ma, G. Wu, X. Zong, Z. Lei, J. Shi, and C. Li, *Journal of Catalysis*, 2009, **266**, 165–168.

117. S. Shen, L. Guo, X. Chen, F. Ren, and S. S. Mao, *International Journal of Hydrogen Energy*, 2010, **35**, 7110–7115.

118. W.-T. Sun, Y. Yu, H.-Y. Pan, X.-F. Gao, Q. Chen, and L.-M. Peng, *Journal of the American Chemical Society*, 2008, **130**, 1124–1125.

119. H. Park, W. Choi, and M. R. Hoffmann, *Journal of Materials Chemistry*, 2008, **18**, 2379.

120. G. Wang, X. Yang, F. Qian, J. Z. Zhang, and Y. Li, *Nano Letters*, 2010, **10**, 1088–1092.

121. M. Moriya, T. Minegishi, H. Kumagai, M. Katayama, J. Kubota, and K. Domen, *Journal of the American Chemical Society*, 2013, **135**, 3733–3735.

122. X. Zong, H. Yan, G. Wu, G. Ma, F. Wen, L. Wang, and C. Li, *Journal of the American Chemical Society*, 2008, **130**, 7176–7.

123. X. Zong, J. Han, G. Ma, and H. Yan, *The Journal of Physical Chemistry C*, 2011, **115**, 12202–12208.

124. Y.-X. Yu, W.-X. Ouyang, Z.-T. Liao, B.-B. Du, and W.-D. Zhang, *ACS applied materials & interfaces*, 2014, **6**, 8467–74.

125. J. Li, S. K. Cushing, P. Zheng, T. Senty, F. Meng, A. D. Bristow, A. Manivannan, and N. Wu, *Journal of the American Chemical Society*, 2014, **136**, 8438–49.

126. X. Wang, C. Liow, D. Qi, B. Zhu, W. R. Leow, H. Wang, C. Xue, X. Chen, and S. Li, *Advanced materials*, 2014, **26**, 3506–12.

127. J. Bang, S. Lee, and J. Jang, *The Journal of Physical Chemistry Letters*, 2012, **3**, 3781–3785.

128. P. Tongying, F. Vietmeyer, D. Aleksiuk, G. J. Ferraudi, G. Krylova, and M. Kuno, *Nanoscale*, 2014, **6**, 4117–24.

129. J. Zhang, S. Z. Qiao, L. Qi, and J. Yu, *Physical chemistry chemical physics*, 2013, **15**, 12088–94.

130. L. Jia, D.-H. Wang, Y.-X. Huang, A.-W. Xu, and H.-Q. Yu, *The Journal of Physical Chemistry C*, 2011, **115**, 11466–11473.

131. Q. Li, B. Guo, J. Yu, J. Ran, B. Zhang, H. Yan, and J. R. Gong, *Journal of the American Chemical Society*, 2011, **133**, 10878–84.

132. Y. P. Xie, Z. B. Yu, G. Liu, X. L. Ma, and H.-M. Cheng, *Energy & Environmental Science*, 2014, **7**, 1895–1901.

133. X. Wang, K. Maeda, A. Thomas, K. Takanabe, G. Xin, J. M. Carlsson, K. Domen, and M. Antonietti, *Nature materials*, 2009, **8**, 76–80.

134. Y. Wang, X. Wang, and M. Antonietti, *Angewandte Chemie International Edition*, 2012, **51**, 68–89.

135. H. W. Kang, S. N. Lim, D. Song, and S. Bin Park, *International Journal of Hydrogen Energy*, 2012, **37**, 11602–11610.

136. L. Ge and C. Han, *Applied Catalysis B: Environmental*, 2012, **117-118**, 268–274.

137. Q. Xiang, J. Yu, and M. Jaroniec, *The Journal of Physical Chemistry C*, 2011, **115**, 7355–7363.

138. Y.-P. Yuan, S.-W. Cao, Y.-S. Liao, L.-S. Yin, and C. Xue, *Applied Catalysis B: Environmental*, 2013, **140-141**, 164–168.

139. H. Yan and H. Yang, *Journal of Alloys and Compounds*, 2011, **509**, L26–L29.

140. Y. Zang, Y. Zuo, and G. Li, *Journal of Materials Chemistry A*, 2014, DOI: 10.1039/C4TA02082K.

141. X. Xu, G. Liu, C. Randorn, and J. T. S. Irvine, *International Journal of Hydrogen Energy*, 2011, **36**, 13501–13507.

142. Y. Wang, R. Shi, J. Lin, and Y. Zhu, *Energy & Environmental Science*, 2011, **4**, 2922–2929.

143. J. Hong, Y. Wang, Y. Wang, W. Zhang, and R. Xu, *ChemSusChem*, 2013, **6**, 2263–2268.

144. Z. Chen, P. Sun, B. Fan, Z. Zhang, and X. Fang, *The Journal of Physical Chemistry C*, 2014, **118**, 7801–7807.

145. L. Yin, Y.-P. Yuan, S.-W. Cao, Z. Zhang, and C. Xue, *RSC Advances*, 2014, **4**, 6127.

146. Y. Fukasawa, K. T. A. Shimojima, M. Antonietti, K. Domen, and T. Okubo, *Chemistry-An Asian Journal*, 2011, **6**, 103–109.

147. L. Ge, F. Zuo, J. Liu, Q. Ma, and C. Wang, *The Journal of Physical Chemistry C*, 2012, 13708–13714.

148. J. Zhang, Y. Wang, J. Jin, J. Zhang, Z. Lin, F. Huang, and J. Yu, *ACS applied materials & interfaces*, 2013, **5**, 10317–24.

149. A. Jorge, D. Martin, M. T. S. Dhanoa, A. S. Rahman, N. Makwana, J. Tang, A. Sella, F. Cora, S. Firth, J. A. Darr, and P. F. McMillan, *The Journal of Physical Chemistry C*, 2013, **117**, 7178–7185.

150. Y. Hou, Z. Wen, S. Cui, X. Guo, and J. Chen, *Advanced Materials*, 2013, **25**, 6291–6297.

151. Y. Hou, F. Zuo, A. P. Dagg, J. Liu, and P. Feng, *Advanced materials*, 2014, DOI: 10.1002/adma.201401032.

152. A. Paracchino, V. Laporte, K. Sivula, M. Grätzel, and E. Thimsen, *Nature materials*, 2011, **10**, 456–461.

153. C. G. Morales-Guio, S. D. Tilley, H. Vrubel, M. Grätzel, and X. Hu, *Nature communications*, 2014, **5**, 3059.

154. C. G. Morales-Guio, L. Liardet, M. T. Mayer, S. D. Tilley, M. Grätzel, and X. Hu, *Angewandte Chemie International Edition*, 2014, DOI: 10.1002/anie.201410569.

155. C.-Y. Lin, Y.-H. Lai, D. Mersch, and E. Reisner, *Chemical Science*, 2012, **3**, 3482–3487.

156. A. Martínez-García, V. K. Vendra, S. Sunkara, P. Haldankar, J. Jasinski, and M. K. Sunkara, *Journal of Materials Chemistry A*, 2013, **1**, 15235.

157. Z. Zhang and P. Wang, *Journal of Materials Chemistry*, 2012, **22**, 2456.

158. M. Wang, L. Sun, Z. Lin, J. Cai, K. Xie, and C. Lin, *Energy & Environmental Science*, 2013, **6**, 1211.

159. Y. Hou, X. Y. Li, Q. D. Zhao, X. Quan, and G. H. Chen, *Applied Physics Letters*, 2009, **95**, 093108.

160. A. D. Handoko and J. Tang, *International Journal of Hydrogen Energy*, 2013, **38**, 13017–13022.

161. E. Pastor, F. M. Pesci, A. Reynal, A. D. Handoko, M. Guo, X. An, A. J. Cowan, D. R. Klug, J. R. Durrant, and J. Tang, *Physical chemistry chemical physics*, 2014, **16**, 5922–6.

162. X. An, K. Li, and J. Tang, *ChemSusChem*, 2014, **7**, 1086–1093.

163. P. D. Tran, S. K. Batabyal, S. S. Pramana, J. Barber, L. H. Wong, and S. C. J. Loo, *Nanoscale*, 2012, **4**, 3875–8.

164. H. Li, X. Zhang, and D. R. MacFarlane, *Advanced Energy Materials*, 2014, DOI: 10.1002/aenm.201401077.

165. Z. Wang, Y. Liu, D. J. Martin, W. Wang, J. Tang, and W. Huang, *Physical chemistry chemical physics*, 2013, **15**, 14956–14960.

166. R. Berera, R. van Grondelle, and J. T. M. Kennis, *Photosynthesis research*, 2009, **101**, 105–118.

167. J. Tang, A. Cowan, J. R. Durrant, and D. R. Klug, *The Journal of Physical Chemistry C*, 2011, **115**, 3143–3150.

168. S. R. Pendlebury, M. Barroso, A. J. Cowan, K. Sivula, J. Tang, M. Grätzel, D. Klug, and J. R. Durrant, *Chemical communications*, 2011, **47**, 716–718.

169. Y. Ma, S. Pendlebury, and A. Reynal, *Chemical Science*, 2014, **5**, 2964–2973.

170. F. Pesci and A. Cowan, *The Journal of Physical Chemistry Letters*, 2011, **2**, 1900–1903.

171. K. Gelderman, L. Lee, and S. Donne, *Journal of chemical education*, 2007, **84**, 685–688.

172. K. G. Upul Wijayantha, S. Saremi-Yarahmadi, and L. M. Peter, *Physical chemistry chemical physics*, 2011, **13**, 5264–70.

173. G. Garcia-Belmonte, *The Journal of Physical Chemistry Letters*, 2013, **4**, 877–886.

174. H. Li, Y. Zhou, L. Chen, W. Luo, Q. Xu, X. Wang, M. Xiao, and Z. Zou, *Nanoscale*, 2013, **5**, 11933–9.

175. J. Zhou, M. Zhang, and Y. Zhu, *Physical Chemistry Chemical Physics*, 2014, **16**, 17627–17633.

176. V. Donchev, K. Kirilov, T. Ivanov, and K. Germanova, *Materials Science and Engineering: B*, 2006, **129**, 186–192.

177. K. Sell, I. Barke, S. Polei, C. Schumann, V. von Oeynhausen, and K.-H. Meiwes-Broer, *Physica Status Solidi (B)*, 2010, **247**, 1087–1094.

178. D. Cavalcoli and A. Cavallini, *Physica Status Solidi (C)*, 2010, **7**, 1293–1300.

179. L. Kronik and Y. Shapira, *Surface Science Reports*, 1999, **37**, 1–206.

180. L. Zhang, T. Jiang, S. Li, Y. Lu, L. Wang, X. Zhang, D. Wang, and T. Xie, *Dalton Transactions*, 2013, **42**, 12998–3003.

181. J. Zhao and F. E. Osterloh, *The Journal of Physical Chemistry Letters*, 2014, **5**, 782–786.

182. J. Wang and F. E. Osterloh, *Journal of Materials Chemistry A*, 2014, **2**, 9405.

183. B. Jiang, Y. Wang, J.-Q. Wang, C. Tian, W. Li, Q. Feng, Q. Pan, and H. Fu, *ChemCatChem*, 2013, **5**, 1359–1367.

184. J. Meng, F. Li, Y. Hu, L. Xu, Z. Sun, and J. Liu, *Materials Research Bulletin*, 2013, **48**, 2111–2116.

185. Y. Lu, Y. Lin, T. Xie, S. Shi, H. Fan, and D. Wang, *Nanoscale*, 2012, **4**, 6393–400.

186. J. Su, X. Zou, G. Li, X. Wei, C. Yan, Y. Wang, J. Zhao, L. Zhou, and J. Chen, *The Journal of Physical Chemistry C*, 2011, **115**, 8064–8071.

187. D. O. Scanlon, C. W. Dunnill, J. Buckeridge, S. A. Shevlin, A. J. Logsdail, S. M. Woodley, C. R. A. Catlow, M. J. Powell, R. G. Palgrave, I. P. Parkin, G. W. Watson, T. W. Keal, P. Sherwood, A. Walsh, and A. A. Sokol, *Nature materials*, 2013, **12**, 798–801.

188. C. R. A. Catlow, Z. X. Guo, M. Miskufova, S. A. Shevlin, A. G. H. Smith, A. A. Sokol, A. Walsh, D. J. Wilson, and S. M. Woodley, *Philosophical transactions. Series A, Mathematical, physical, and engineering sciences*, 2010, **368**, 3379–3456.

189. X. Han, H. Morgan Stewart, S. A. Shevlin, C. R. A. Catlow, and Z. X. Guo, *Nano letters*, 2014, **14**, 4607–4614.

190. J. Meyer, P. R. Kidambi, B. C. Bayer, C. Weijtens, A. Kuhn, A. Centeno, A. Pesquera, A. Zurutuza, J. Robertson, and S. Hofmann, *Scientific Reports*, 2014, **4**, 5380.

191. K. Steiner, W. Chen, and A. Pasquarello, *Physical Review B*, 2014, **89**, 205309.

192. S. A. Shevlin and Z. X. Guo, *Chemical Society Reviews*, 2009, **38**, 211–225.

193. P. Liao and E. A. Carter, *Chemical Society Reviews*, 2013, **42**, 2401–2422.

194. J. P. Perdew and M. Levy, *Physical Review Letters*, 1983, **51**, 1884–1887.

195. J. L. Gavartin, P. V Sushko, and A. L. Shluger, *Physical Review B*, 2003, **67**, 035108.

196. V. I. Anisimov, J. Zaanen, and O. K. Andersen, *Physical Review B*, 1991, **44**, 943–954.

197. J. P. Perdew, K. Burke, and M. Ernzerhof, *Physical Review Letters*, 1996, **77**, 3865–3868.

198. J. P. Perdew, M. Emzerhof, and K. Burke, *Journal of Chemical Physics*, 1996, **105**, 9982–9985.

199. M. Ernzerhof and G. E. Scuseria, *Journal of Chemical Physics*, 1999, **110**, 5029–5036.

200. J. Heyd, G. E. Scuseria, and M. Ernzerhof, *Journal of Chemical Physics*, 2003, **118**, 8207–8215.

201. S. A. Shevlin and S. M. Woodley, *Journal of Physical Chemistry C*, 2010, **114**, 17333–17343.

202. E. Berardo, H.-S. Hu, S. A. Shevlin, S. M. Woodley, K. Kowalski, and M. A. Zwijnenburg, *Journal of Chemical Theory and Computation*, 2014, **10**, 1189–1199.

203. S. G. Li and D. A. Dixon, *Journal of Physical Chemistry A*, 2008, **112**, 6646–6666.

204. J. Ihm, A. Zunger, and M. L. Cohen, *Journal of Physics C-Solid State Physics*, 1979, **12**, 4409–4422.

205. A. Walsh and K. T. Butler, *Accounts of Chemical Research*, 2014, **47**, 364–372.

206. Z. Zhang and J. T. Yates Jr., *Chemical Reviews*, 2012, **112**, 5520–5551.

207. J. P. Bosco, D. O. Scanlon, G. W. Watson, N. S. Lewis, and H. A. Atwater, *Journal of Applied Physics*, 2013, **113**.

208. L. A. Burton and A. Walsh, *Applied Physics Letters*, 2013, **102**.

209. S.-H. Yoo, A. Walsh, D. O. Scanlon, and A. Soon, *Rsc Advances*, 2014, **4**, 3306–3311.

210. A. Walsh and C. R. A. Catlow, *Journal of Materials Chemistry*, 2010, **20**, 10438–10444.

211. Y. Hinuma, F. Oba, and I. Tanaka, *Physical Review B*, 2013, **88**, 075319.

212. P. G. Moses, M. Miao, Q. Yan, and C. G. Van de Walle, *Journal of Chemical Physics*, 2011, **134**.

213. J. Kang, S. Tongay, J. Zhou, J. B. Li, and J. Q. Wu, *Applied Physics Letters*, 2013, **102**.

214. L. Sun, Y. Qi, C.-J. Jia, Z. Jin, and W. Fan, *Nanoscale*, 2014, **6**, 2649–2659.

215. L. Wang, J. Ge, A. Wang, M. Deng, X. Wang, S. Bai, R. Li, J. Jiang, Q. Zhang, Y. Luo, and Y. Xiong, *Angewandte Chemie-International Edition*, 2014, **53**, 5107–5111.

216. C. A. Downing, A. A. Sokol, and C. R. A. Catlow, *Physical Chemistry Chemical Physics*, 2014, **16**, 184–195.

217. S. Metz, J. Kastner, A. A. Sokol, T. W. Keal, and P. Sherwood, *Wiley Interdisciplinary Reviews-Computational Molecular Science*, 2014, **4**, 101–110.

218. V. Pfeifer, P. Erhart, S. Li, K. Rachut, J. Morasch, J. Broetz, P. Reckers, T. Mayer, S. Ruehle, A. Zaban, I. Mora Sero, J. Bisquert, W. Jaegermann, and A. Klein, *Journal of Physical Chemistry Letters*, 2013, **4**, 4182–4187.

219. P. Deak, B. Aradi, and T. Frauenheim, *Journal of Physical Chemistry C*, 2011, **115**, 3443–3446.

220. A. A. Sokol, S. A. French, S. T. Bromley, C. R. A. Catlow, H. J. J. van Dam, and P. Sherwood, *Faraday Discussions*, 2007, **134**, 267–282.

221. N. R. D'Amico, G. Cantele, and D. Ninno, *Applied Physics Letters*, 2012, **101**, 141606.

222. C. G. Van De Walle and R. M. Martin, *Physical Review B*, 1986, **34**, 5621–5634.

223. S. H. Wei and A. Zunger, *Applied Physics Letters*, 1998, **72**, 2011–2013.

224. J. M. Bass, M. Oloumi, and C. C. Matthai, *Journal of Physics-Condensed Matter*, 1989, **1**, 10625–10628.

225. M. Zemzemi and S. Alaya, *Superlattices and Microstructures*, 2013, **64**, 311–318.

226. Z. Romanowski, P. Kempisty, K. Sakowski, P. Strak, and S. Krukowski, *Journal of Physical Chemistry C*, 2010, **114**, 14410–14416.

227. D. Cociorva, W. G. Aulbur, and J. W. Wilkins, *Solid State Communications*, 2002, **124**, 63–66.

228. Y.-H. Li, A. Walsh, S. Chen, W.-J. Yin, J.-H. Yang, J. Li, J. L. F. Da Silva, X. G. Gong, and S.-H. Wei, *Applied Physics Letters*, 2009, **94**.

229. M. Ichimura, *Solar Energy Materials and Solar Cells*, 2009, **93**, 375–378.

230. W. Bao and M. Ichimura, *Japanese Journal of Applied Physics*, 2012, **51**, 061203.

231. Z.-Y. Dong, Y.-F. Li, B. Yao, Z.-H. Ding, G. Yang, R. Deng, X. Fang, Z.-P. Wei, and L. Liu, *Journal of Physics D-Applied Physics*, 2014, **47**, 075304.

232. S. A. Chambers, T. Ohsawa, C. M. Wang, I. Lyubinetsky, and J. E. Jaffe, *Surface Science*, 2009, **603**, 771–780.

233. A. M. Haleem and M. Ichimura, *Journal of Applied Physics*, 2010, **107**, 034507.

234. H. Seo, A. B. Posadas, C. Mitra, A. V Kvit, J. Ramdani, and A. A. Demkov, *Physical Review B*, 2012, **86**, 9.

235. M. Peressi, N. Binggeli, and A. Baldereschi, *Journal of Physics D-Applied Physics*, 1998, **31**, 1273–1299.

236. W. Wang, W. Yang, R. Chen, X. Duan, Y. Tian, D. Zeng, and B. Shan, *Physical Chemistry Chemical Physics*, 2012, **14**, 2450–2454.

237. M. Ribeiro, L. R. C. Fonseca, and L. G. Ferreira, *Epl*, 2011, **94**, 27001.

238. M. Ribeiro, L. G. Ferreira, L. R. C. Fonseca, and R. Ramprasad, *Materials Science and Engineering B-Advanced Functional Solid-State Materials*, 2012, **177**, 1460–1464.

239. O. P. Silva, M. Ribeiro, R. R. Pela, L. K. Teles, L. G. Ferreira, and M. Marques, *Journal of Applied Physics*, 2013, **114**, 033709.

240. M. Ribeiro, L. R. C. Fonseca, and L. G. Ferreira, *Physical Review B*, 2009, **79**, 241312.

241. W. C. Wang, S. Y. Chen, P. X. Yang, C. G. Duan, and L. W. Wang, *Journal of Materials Chemistry A*, 2013, **1**, 1078–1085.

242. M. A. L. Marques, J. Vidal, M. J. T. Oliveira, L. Reining, and S. Botti, *Physical Review B*, 2011, **83**, 035119.

243. R. Ramprasad, H. Zhu, P. Rinke, and M. Scheffler, *Physical Review Letters*, 2012, **108**, 066404.

244. J. Conesa, *The Journal of Physical Chemistry C*, 2012, **116**, 18884–18890.

245. L. Liu, Z. Ji, W. Zou, X. Gu, Y. Deng, F. Gao, C. Tang, and L. Dong, *Acs Catalysis*, 2013, **3**, 2052–2061.

246. M. Nolan, *Physical Chemistry Chemical Physics*, 2011, **13**, 18194–18199.

247. L. I. Bendavid and E. A. Carter, *Surface Science*, 2013, **618**, 62–71.

248. T. Minegishi, N. Nishimura, J. Kubota, and K. Domen, *Chemical Science*, 2013, **4**, 1120–1124.